

An aerial photograph of a desert landscape. In the foreground and middle ground, there are several large, rectangular solar panel arrays arranged in rows. The terrain is arid and hilly, with a dark green reservoir or lake visible on the right side. The sky is clear and blue.

# Infrared optical filters for passive cooling of c-Si solar modules

Patricia Seoane da Silva

Technische Universiteit Delft

TECHNISCHE UNIVERSITEIT DELFT

MASTER THESIS

---

# Infrared optical filters for passive cooling of photovoltaic modules

---

*Author:*  
Patricia Seoane da Silva  
4503082

*Supervisors:*  
Dr. ir. Olindo Isabella  
ir. Juan Camilo Ortiz Lizcano

*A thesis submitted in partial fulfillment of the requirements  
for the degree of MSc Sustainable Energy Technology*

*in the*

Photovoltaic Material and Devices Group  
TU Delft

to be defended publicly on Monday September 11, 2017 at 13:00 PM.

Thesis committee: Dr. ir. Olindo Isabella, TU Delft  
Prof. Dr. ir. Miro Zeman, TU Delft  
Dr. ir. Ivan Buijnsters, TU Delft



*A man dereita á dereita do corpo,  
a man esquerda á esquerda.  
En plenas facultades,  
teño a cabeza no centro do mundo  
e voulle cambiando os argumentos  
ós meus soños escasos e prudentes.*

—Lois Pereiro, *Revisando os danos*



TECHNISCHE UNIVERSITEIT DELFT

# *Abstract*

EEMCS Faculty

TU Delft

MSc Sustainable Energy Technology

## **Infrared optical filters for passive cooling of photovoltaic modules**

by Patricia Seoane da Silva

4503082

The performance of a photovoltaic (PV) module is considerably affected by its operating temperature. This is mainly due to a negative thermal coefficient that causes the open circuit voltage to decrease as the temperature rises beyond the standard. In recent years, several approaches have been proposed in order to tackle this problem. Some representative examples are hybrid photovoltaic-thermal devices or floating installations in which modules are in direct contact with water. However, these are active solutions that require an additional support and therefore extensive engineering integration.

Within this context, this thesis proposes a novel method for passively reducing the operating temperature of photovoltaic modules. This is based on the use of optical filters to block undesired components of light in the infrared. At these wavelengths, the energy of the photons absorbed is not sufficient to overcome the bandgap of the cell, and hence it only accounts for a heat source within the module.

In order to design the filter, a thermal model has been firstly developed in COMSOL Multiphysics. The purpose of this study was to evaluate the progressive increase in the module temperature due to absorption of light at different wavelengths. These simulations revealed that a complete reflection of light between 1100-2500 nm could decrease the module temperature by around 5 to 6 °C. Based on this result, an optical filter was designed accordingly. This was made following different approaches, from standard optical theory to refined optimization methods. Finally, various test filters were designed and different strategies for their deposition were evaluated.



## Acknowledgements

This thesis is the culmination of one year of work at the Photovoltaic Materials and Devices group of TU Delft. This would not have been possible without the help of all the personal involved in the group.

First of all, I would like to thank Dr. Olindo Isabella for giving me the chance to work in this project. A year ago I was full of insecurities, trying to figure out what I really wanted to do. Thank you, Olindo, for listening to me and helping me find a topic that was suited to my interests. I would also like to thank you for your supervision, kindness and, more importantly, patience throughout this year.

Special thanks to Juan Camilo for helping me during these last months. I wish you the best of luck during your PhD research and hope that you continue to inspire future students and transmit them your optimism.

On the other hand I would like to thank all the researchers and technical staff of the PVMD department. I really appreciate that you took the time to help me at different points of this project.

I am also thankful to Prof. Dr. ir. Miro Zeman and Dr. ir. Ivan Buijnsters for being part of my thesis committee.

On a personal level, I would like to thank all the people that made my time in Delft a bit less grey. Special thanks to all of those who prolonged the coffee time after lunch, shared a beer sometime and kept me distracted from the university drama. I could not have done this without your support.

Thanks to my family, who always supported me and gave me the strength I needed in times of weakness. This past year was full of ups and downs, but you never stopped encouraging me to pursue my dreams. I cannot express how thankful I am for that. *Graciñas papá, mamá e Edu.*

But most importantly, thank you, Carlos. For sharing these two years with me, for all the walks along the canal, the great music, the Christmas lights, the morning coffee, etc. Thank you for telling me that everything was going to be ok, for supporting me and making me believe in myself even in my worst behavior (*por non dicir cando estaba repugnante!*). *God only knows what I'd be without you.*



# Contents

<b>Abstract</b>	<b>v</b>
<b>Acknowledgements</b>	<b>vii</b>
<b>1 Introduction</b>	<b>1</b>
1.1 Background . . . . .	1
1.2 Solar energy . . . . .	2
1.2.1 Operating principle of a solar cell . . . . .	3
1.2.2 Crystalline silicon technology . . . . .	4
1.2.3 Losses and efficiency limits . . . . .	6
1.3 Large scale photovoltaic installations . . . . .	7
1.3.1 Overview . . . . .	8
1.3.2 Operational aspects on LSPV . . . . .	10
1.4 Objective and outline of the thesis . . . . .	11
<b>2 Temperature management in solar cells</b>	<b>13</b>
2.1 Electrical parameters of solar cells . . . . .	13
2.2 Influence of temperature on PV module performance . . . . .	14
2.3 State-of-the-art . . . . .	16
<b>3 Thermal model</b>	<b>19</b>
3.1 Heat exchange mechanisms . . . . .	19
3.1.1 Conduction . . . . .	20

3.1.2	Convection	20
3.1.3	Radiation	23
3.2	Ray tracing	25
3.2.1	Reference configuration	25
3.3	Implementation	26
3.3.1	Overview	27
3.3.2	Model definition	27
3.3.3	Heat sources within the module	32
3.3.4	Validation	34
<b>4</b>	<b>Application of the thermal model</b>	<b>37</b>
4.1	Definition of heat sources	37
4.2	Optimum wavelength range	39
4.3	Potential benefit	41
<b>5</b>	<b>Optical filters</b>	<b>47</b>
5.1	Optics in multilayer structures	47
5.1.1	Interaction of light with a medium	47
5.1.2	Influence of coatings	49
5.1.3	Modeling of multilayer structures	50
5.2	Optical filters	51
5.3	Distributed Bragg Reflectors	52
5.4	Needle technique	55
5.5	Fence Post Method	56
<b>6</b>	<b>Experimental setup</b>	<b>59</b>
6.1	Thermal evaporator: PROVAC	59
6.2	Spectroscopic ellipsometry	60
6.3	Determination of reflection, absorption and transmission: Lambda	60

<b>7 Design and fabrication of the optical filter</b>	<b>63</b>
7.1 Optical filter design . . . . .	63
7.1.1 Selection of materials . . . . .	63
7.1.2 Preliminary designs . . . . .	66
7.1.3 Construction of the test filter . . . . .	71
7.1.4 Discussion . . . . .	73
7.1.5 Alternative methods . . . . .	75
<b>8 Conclusions and recommendations</b>	<b>77</b>



# List of Figures

1.1	Primary energy consumption by fuel from 1980 and projections for 2040.	1
1.2	ASTM reference spectra.	3
1.3	Schematic representation of the working principle of a solar cell.	4
1.4	Schematic representation of a c-Si solar cell.	5
1.5	Components of a typical c-Si solar module.	6
1.6	Fraction of the AM 1.5 spectrum that can be converted into usable energy in a crystalline silicon solar cell.	7
1.7	Aerial view of a solar farm in Nyngan, Australia	8
1.8	Installed PV capacity in the U.S. from 2010 until the present. Forecasted (E) values included until 2022.	9
1.9	Operable utility-scale PV in the United States. Data for 2015.	10
2.1	Effect of temperature and incident irradiance on the I-V curve of a solar cell	14
2.2	Examples of active cooling mechanisms.	16
3.1	Schematic representation of conduction, convection and radiation.	19
3.2	Radiation at a surface of two different media.	24
3.3	Reference solar module configuration for the optical simulations in Gen-Pro4.	25
3.4	Flow chart of the thermal model.	27
3.5	Mini-module configuration simulated in COMSOL.	28
3.6	Detail of the geometry built in COMSOL. The transparency effect reveals the presence of busbars and fingers.	28
3.7	Time dependency evaluation in a standard PV module.	29

3.8	Silver front metallization. Conventional H-pattern grid comprised of 2 busbars and 30 fingers. . . . .	30
3.9	Normal size mesh generated in COMSOL. . . . .	31
3.10	Heat exchange mechanisms around a photovoltaic module. . . . .	31
3.11	Representation of efficiency values. . . . .	33
3.12	Comparison of the simulated (lines) and measured (symbols) module temperature for different irradiance levels. . . . .	34
4.1	Fractions of the solar spectrum transmitted, absorbed and reflected in the constituent layers of a c-Si PV module. . . . .	38
4.2	Spectral absorption in the constituent layers of a PV module. . . . .	38
4.3	Increase in the module temperature due to light absorption along the solar spectrum. . . . .	39
4.4	Heat power inputs to the thermal model. . . . .	40
4.5	Module temperature as a function of the cumulative wavelength (i.e. maximum limit of absorption). . . . .	41
4.6	Module temperature in two representative days in Rotterdam (The Netherlands). . . . .	42
4.7	Module temperature in two representative days in Palermo (Italy). . . . .	43
4.8	Percentage increase in the annual energy yield as a function of average wind speed and direct normal irradiance. . . . .	45
5.1	Reflected and refracted portions of light at the interface between two mediums. . . . .	48
5.2	Interference effect. Schematic representation of a case of constructive interference. . . . .	49
5.3	Interference effect. . . . .	50
5.4	Paths of light with it reaches a multilayer structure. . . . .	50
5.5	Operating principle of two different optical filters which favor the transmission of the green component of light. . . . .	51
5.6	Transmission curves for different types of dichroic filters. . . . .	52
5.7	Reflectance at $\lambda_B$ as a function of DBR pairs. . . . .	54
5.8	Reflectance of a DBR for different number of pairs. . . . .	54
5.9	Reflectance profile of different photonic crystal structures. . . . .	55

5.10	Iteration scheme of the needle technique method . . . . .	56
5.11	Index of refraction as a function of thickness for a typical Fence Post design.	57
6.1	Schematic representation of the deposition chamber in PROVAC . . . . .	59
6.2	Schematic representation of an spectrophotometer. . . . .	61
7.1	Titanium dioxide phase transition diagram a function of annealing temperature. . . . .	64
7.2	Refractive index of titanium dioxide deposited via thermal and electron beam evaporation. . . . .	64
7.3	Extinction coefficient of titanium dioxide deposited via thermal and electron beam evaporation. . . . .	65
7.4	Titanium dioxide phase transition diagram a function of annealing temperature. . . . .	66
7.5	Reflectance profile of an infrared filter based on three modulated Bragg reflectors. . . . .	67
7.6	Influence of a modulated optical filter over the performance of a solar cell.	68
7.7	Reflectance profile of a 156 layer optical filter optimized via needle technique. . . . .	69
7.8	Reflectance profile of a 92 layer optical filter optimized via needle technique. . . . .	69
7.9	Reflectance profile of a 44 layer optical filter optimized via needle technique. . . . .	70
7.10	Reflectance profile of a 20 layer optical filter optimized via needle technique. . . . .	71
7.11	Stress in a flat-glass substrate sample after the deposition of seven layers. Some particle remains can be seen on the lateral side. . . . .	72
7.12	Stress in the samples after the deposition of eight layers. . . . .	73
7.13	Surface figure of a $\text{TiO}_2/\text{MgF}_2$ stack. . . . .	73
7.14	Color degradation in a multilayer structure based on magnesium fluoride and titanium dioxide. This effect indicates that the surface is not uniform. . . . .	74
7.15	Reflectance profile of a 18 layer optical filter optimized via the Fence Post method. . . . .	75

7.16 Reflectance profile of an infrared filter based on silicon nitride and silicon oxide. . . . . 76

# List of Tables

3.1	Physical parameters used for the thermal simulation. . . . .	30
4.1	Effect of an infrared optical filter in a PV system in Rotterdam (The Netherlands). . . . .	42
4.2	Effect of an infrared optical filter in a PV system in Palermo (Italy). . . . .	43
4.3	Effect of an infrared optical filter in a PV system in Tucson, Arizona (United States). . . . .	44
4.4	Effect of an infrared optical filter in a PV system in Barrancabermeja (Colombia). . . . .	44
7.1	Specifications of an optical filter based on three modulated Bragg reflectors. The high and low refractive index materials are titanium dioxide and magnesium fluoride. . . . .	67



## List of Abbreviations

<b>AM</b>	Air Mass
<b>ARC</b>	Anti-reflective coating
<b>BSF</b>	Back Surface Field
<b>c-Si</b>	Crystalline silicon
<b>DBR</b>	Distributed Bragg Reflector
<b>EVA</b>	Encapsulant (ethyl vinyl acetate)
<b>IR</b>	Infrared
<b>LSPV</b>	Large Scale Photovoltaic Installations
<b>PECVD</b>	Plasma Enhanced Chemical Vapor Deposition
<b>PV</b>	Photovoltaic
<b>PVF</b>	Polyvinyl fluoride
<b>PVT</b>	Photovoltaic Thermal Collector
<b>QWOT</b>	Quarter wavelength optical thickness
<b>SE</b>	Spectroscopic ellipsometry
<b>STC</b>	Standard Test Conditions
<b>UV</b>	Ultraviolet



# Physical Constants

Stefan-Boltzmann constant  $\sigma = 5.67 \times 10^{-8} \text{ W m}^{-2} \text{ K}^{-4}$   
Boltzmann constant  $k_{\text{B}} = 1.38 \times 10^{-23} \text{ J K}^{-1}$



## List of Symbols

$A$	Absorption coefficient	-
$A_{ac}$	Active area	-
$A_{gr}$	Non-active area	-
$C_p$	Heat capacity	$\text{J kg}^{-1} \text{K}$
$E$	Emitted power	$\text{W m}^{-2} \text{nm}^{-1}$
$E_C$	Conduction band edge	eV
$E_G$	Energy of the bandgap	eV
$E_V$	Valence band edge	eV
FF	Fill factor	-
$G$	Irradiance	$\text{W m}^{-2}$
Gr	Grashof number	-
$h$	Convective heat transfer	$\text{W m}^{-2} \text{K}^{-1}$
$I_{sc}$	Short circuit current	A
$J_{sc}$	Short circuit current density	$\text{A m}^{-2}$
$k$	Extinction coefficient	-
$Q$	Heat power	$\text{W m}^{-2}$
$n$	Refractive index	-
Nu	Nusselt number	-
$P$	Power	W
$Pr$	Prandtl number	-
$q''$	Heat flux	$\text{W m}^{-2}$
$R$	Reflectance	-
$T$	Temperature	$^{\circ}\text{C}, \text{K}$
$V_{oc}$	Open circuit voltage	V
$\alpha$	Absorption	-
$\eta$	Efficiency	-
$\kappa$	Thermal conductivity	$\text{W m}^{-2} \text{K}^{-1}$
$\varepsilon$	Emissivity	-
$\rho$	Density	$\text{kg m}^{-3}$
$\lambda$	Wavelength	nm
$\theta$	angle of incidence	rad



# Chapter 1

## Introduction

### 1.1 Background

Over the past years, human energy consumption has increased sharply on account of population growth. Indeed, in 2015 the world population reached 7.3 billion people and this number is expected to increase by more than one billion within the next 15 years [1]. Together with the increasing living standards, this has put additional strain in the energy supply.

This situation raises the question of whether there are sufficient energy resources to fulfil the world demand. Traditionally, society has relied on the use of fossil fuels (namely petroleum, natural gas and coal) for this purpose (Figure 1.1). However, the continued use of these energy sources is not compatible with their generation cycle and, as a consequence, they are becoming depleted.

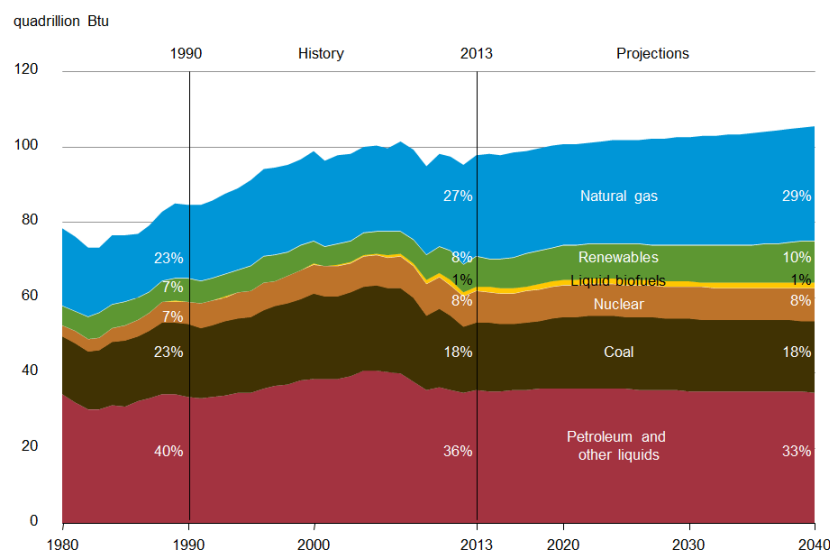


Figure 1.1: Primary energy consumption by fuel from 1980 and projections for 2040. Extracted from [2].

In addition to this, burning fossil fuels has detrimental consequences over the Earth's

climate system due to the production of greenhouse gases (GHG). In fact, human activity has led to a substantial increase in the amount of carbon dioxide, methane and nitrous oxides emitted to the atmosphere. This has enhanced the natural greenhouse effect of the planet and, in consequence, motivated an increase in the temperature of the surface and oceans. Moreover, the global water cycle has been altered and the Greenland Ice Sheet has started to melt, causing together a notable rise in the sea level [3].

Under these circumstances, it is evident that only by adopting renewable and sustainable forms of energy generation the increasing energy demand can be compensated. To this regard, even though different renewable energy technologies are expected to contribute to the total energy share, solar photovoltaic (PV) is considered to be one of the most promising ones for the upcoming years. Indeed, the installed PV capacity has experienced a notable increase since 2010 and it is expected to account for a 16% of the global electricity share by 2050 [4]. This rapid success has been mainly favoured by the decrease in the associated costs of the technology. From 2010 the cost of a PV module and of a full PV system has been divided by a factor of five and three respectively. In addition, the levelised cost of electricity (LCOE) is already below retail electricity prices in several countries and is approaching the level of generation costs from conventional alternatives [4].

On the other hand, the performance of different PV technologies has also been improved throughout the past decade. For instance, the average efficiency of commercial silicon modules has increased at a ratio of about 0.3% per year. In addition to their higher efficiencies, modules are nowadays able to operate during higher time frames. In fact, a lifetime of around 25 and 30 years is frequently guaranteed (at a minimum of 80-70% of their rated output) [4].

## 1.2 Solar energy

The extreme pressure and temperature conditions in the core of the Sun enable fusion reactions to occur. As a result, energy is produced and transmitted firstly from the core to the photosphere (visible surface of the Sun) and then to the Earth's surface in form of thermal radiation [5]. However, not all the incoming radiation can be effectively harvested. This is due to the fact that as radiation passes through the atmosphere, a substantial fraction is scattered and absorbed by air molecules, dust particles and/or aerosols. In addition, depending on the location and the relative position of the Earth with respect to the Sun, the intensity of the solar irradiation received is different [6].

The fluctuations on the incoming solar irradiation hamper the comparison between different solar cells performance. In order to tackle this issue, the American Society for Testing and Materials (ASTM) developed a standard condition for the cells to be tested [7]. As illustrated in Figure 1.2, there are three reference spectra namely AM 0, AM 1.5 G and AM 1.5 D. In this notation, AM stands for *air mass* and is referred to the ratio between the distance that the sunlight has to travel to reach a certain location and the minimal possible path (when Sun is at the zenith). The only exception to this rule is the AM 0 spectrum, which is the irradiance distribution outside the atmosphere.

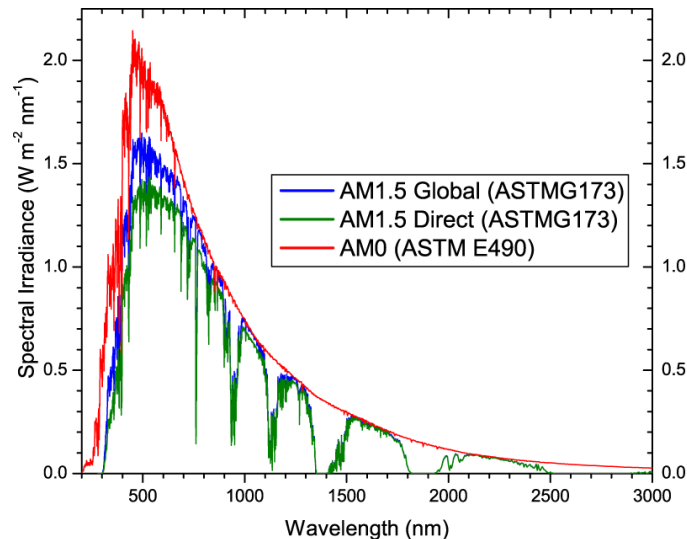


Figure 1.2: ASTM reference spectra. Adapted from [8].

Generally, solar cells are tested at 25 °C under the AM 1.5 G spectrum. That is, under global irradiance and in a 37° tilted sun-facing surface. This implies that the standard incident power is 1000 W/m<sup>2</sup>.

### 1.2.1 Operating principle of a solar cell

Once the irradiance levels at the Earth's surface have been established, it is possible to analyze how this energy is harvested and converted into electricity in a solar cell. In this section, an overview of this process is presented and further insight is given for the particular case of crystalline silicon (c-Si) devices.

The operating principle of a solar cell is based on the *photovoltaic effect*, i.e. generation of a potential difference in a material upon exposure to light [6]. More specifically, when light photons are absorbed their energy is used to excite an electron from an initial energy level ( $E_i$ ) to a higher energy one ( $E_f$ ).

In an ideal semiconductor material, electrons can occupy energy levels below the valence band edge ( $E_V$ ) and above the conduction band edge ( $E_C$ ). Between the two bands, no allowed energy states exist to be populated by electrons. Therefore, only photons with an energy larger than the difference between these two bands—generally known as *band gap* ( $E_G$ )— can be used to excite an electron from the valence band to the conduction band and thus generate an electron-hole pair (also known as energy carriers).

Without external support, these energy carriers generated are likely to recombine and release the energy absorbed. For this reason, solar cells are equipped with semipermeable membranes (generally  $n$  and  $p$ -type materials) at both sides of the absorption region. This guarantees that electrons and holes are individually collected at opposite points of the cell. After separation, the electrons are extracted from the solar cells by means of electrical contacts so that they can finally perform work in an external circuit.

An schematic view of the working principle of a solar cell is depicted in Figure 1.3. As can be seen, Figure 1.3a represents the transmission of energy from a photon ( $E_{ph}$ ) to an electron so that it can overcome the energy bandgap, leading to the generation of an electron-hole pair. After that, Figure 1.3b shows how the charge carriers first are collected at the extremes of the cell and then perform work in the external circuit.

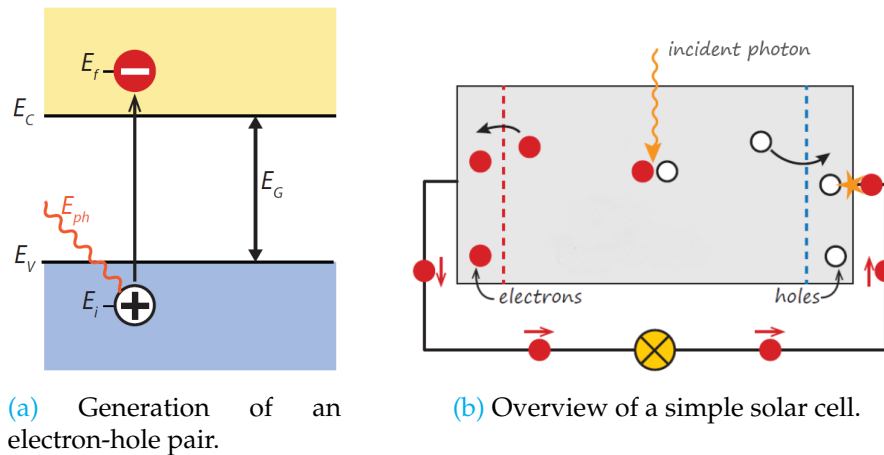


Figure 1.3: Schematic representation of the working principle of a solar cell. Adapted from [6].

## 1.2.2 Crystalline silicon technology

Crystalline silicon (specially on its multi-crystalline form) has been the leading solar cell technology over the past years, accounting for a market share of more than 90%. This trend is expected to continue until at least 2020, with a forecasted share of around 50% [9].

The most conventional type of silicon solar cell is presented in Figure 1.4. As can be seen, the bulk of this structure is an uniformly doped  $p$ -type silicon wafer, which is commonly known as *absorber*. On top of it, a thin  $n$ -type region or *emitter* is created by means of indiffusion of a doping agent (e.g. phosphorus) into the silicon bulk. In terms of sizing, the entire wafer has a thickness between 150 and 200  $\mu\text{m}$ , among which the emitter only accounts for around 0.3  $\mu\text{m}$  of the total [6].

As explained in the previous section, the generated electron-hole pairs move towards the  $n$  and  $p$ -regions and are finally collected at the front and back contacts of the cell. In standard devices, these are a fine silver grid and a thin aluminum film screen printed to the back. This last process is particularly interesting because it causes the appearance of a heavily  $p$ -doped region in between the silicon bulk and the aluminum contact, referred in Figure 1.4 as *back surface field*, BSF. This is done in order to minimize possible recombination losses at the back of the cell and hence increase the collection efficiency [6, 10].

Finally, a frequent element in standard c-Si based solar cells is the anti-reflective (ARC) coating. In most of the cases, this is a textured silicon nitride film which not only leads to a reduction in the reflection losses, but also acts as a passivation layer, hence reducing the recombination at the front side of the cell due to structural defects.

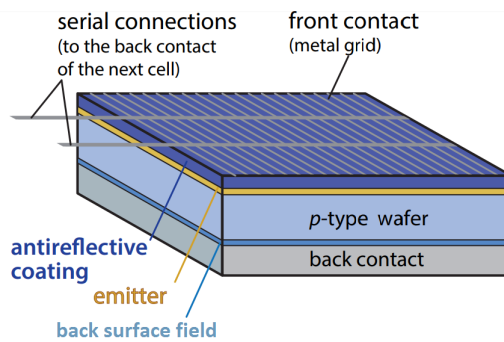
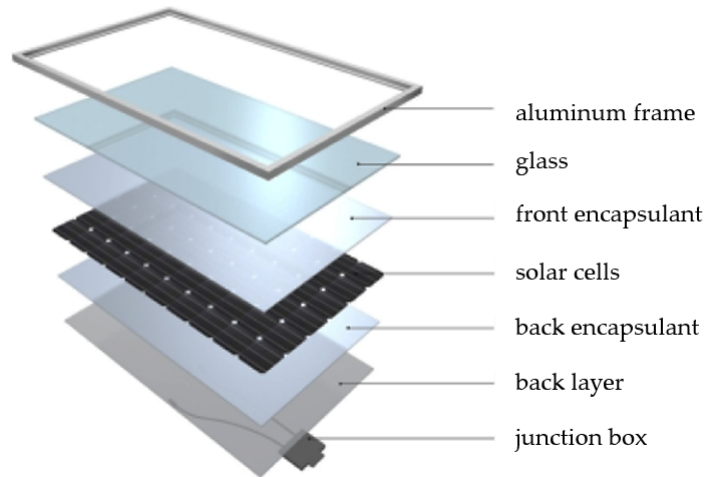


Figure 1.4: Schematic representation of a crystalline silicon solar cell. Adapted from [6].

Approximately 60 to 96 of these solar cells are required to manufacture a single crystalline silicon module. Normally, the cells are firstly connected in series and then sandwiched in between some additional layers. These might change slightly depending on the manufacturer, however, modern silicon based modules are generally comprised of the following elements (also depicted in Figure 1.5):

- *Glass*. This layer provides mechanical stability and guarantees that light is effectively transported towards the solar cells. In order to do so, varieties with low iron content are generally used, since this could lead to unwanted absorption in the layer.
- *Encapsulant*. Two layers of an encapsulant material are used to provide adhesion between the solar cells, and the top and rear surface of the module. In the majority of cases, this is *ethyl vinyl acetate* or EVA.
- *Rear surface*. The objective of this last layer is to act as a barrier against humidity and other stresses. In most of the cases, this surface is made of a combination of polyvinyl fluoride (PVF) and polyester in the form of PVF-polyester-PVF. This is generally known by the name of the brand which produces it, Tedlar®



**Figure 1.5:** Components of a typical c-Si solar module. Adapted from [11].

### 1.2.3 Losses and efficiency limits

It can be proven that the maximum theoretical efficiency of a single junction c-Si solar cell is around 29% [12]. This is mainly due to the fact that only a fraction of the AM 1.5 spectrum can be converted into usable energy [6].

Indeed, in order to successfully generate an electron-hole pair, the incident photons must have an energy equal or higher than the bandgap of the semiconductor material. This type of loss is known as *spectral mismatch* and for the particular case of crystalline ( $E_G = 1.12$  eV) it implies that absorption only occurs in the ultraviolet (UV) and visible part of the spectrum (Figure 1.6). Hence infrared light cannot possibly be harvested.

On the other hand, when the energy content of the absorbed photons is higher than the bandgap, the remaining energy is released as heat. This last phenomenon—generally known as *thermalization*—not only implies that a fraction of energy is being lost, but also that the module is susceptible to warm up. As will be explained later on, this can eventually cause the cell performance to decrease.

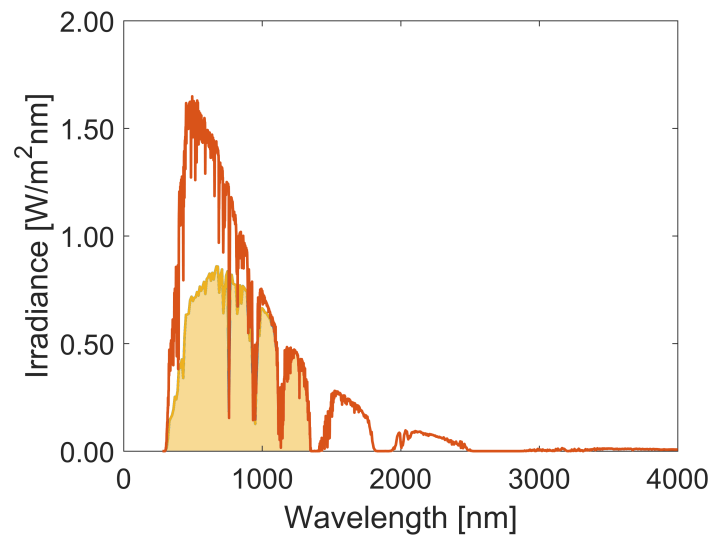


Figure 1.6: Fraction of the AM 1.5 spectrum that can be converted into usable energy in a crystalline silicon solar cell.

Apart from the spectral mismatch losses, there are several factors that condition the performance of a solar cell. For instance, parts of the incident irradiance can be reflected either at some of the module's interface or at the front contact of the cell. In addition, not all the charge carriers generated are collected in the electrodes due to recombination in the bulk, at the interfaces and/or at the surfaces of the junction [6].

### 1.3 Large scale photovoltaic installations

Large scale photovoltaic installations (often shortened as LSPV) account for an important fraction of the total PV capacity installed over the past decade [13]. As revealed in Figure 1.7, the number of modules in these facilities is enormous. In particular, it can oscillate between hundreds of thousands to even millions; making the electricity production levels in these plants to be extremely high. For this reason, LSPV plants are an excellent reference to simulate the impact of a newly developed technology, since it would reveal whether its contribution to the plant energy generation is worth it or not.



**Figure 1.7:** Aerial view of a solar farm in Nyngan, Australia. Obtained from [14].

Based on this, the objective of this section is to provide an overview of modern LSPV installations in terms of capacity and operational aspects. This should be used as a reference for further improvements and simulations.

### 1.3.1 Overview

The first utility-scale photovoltaic power plants were constructed and commissioned in the late seventies and early eighties respectively. These installations served mainly as pilot plants for different R&D programmes in the United States and Europe and hence their energy capacity was always kept at a low value; generally between 100 and 300 kW [15].

However, these pioneering projects were quite successful and ultimately paved the way for the construction and operation of larger installations. As a matter of fact, the number and capacity of LSPV plants has progressively increased since that moment. This upward trend is illustrated in Figure 1.8, in which annual values for the installed PV capacity in the U.S. are plotted. As can be seen, the number of utility-scale installations has increased sharply over the past years and is expected to continue to do so during the upcoming years. In addition, LSPV has consolidated itself as the most important PV application, ahead of residential and non-residential applications [13, 15].

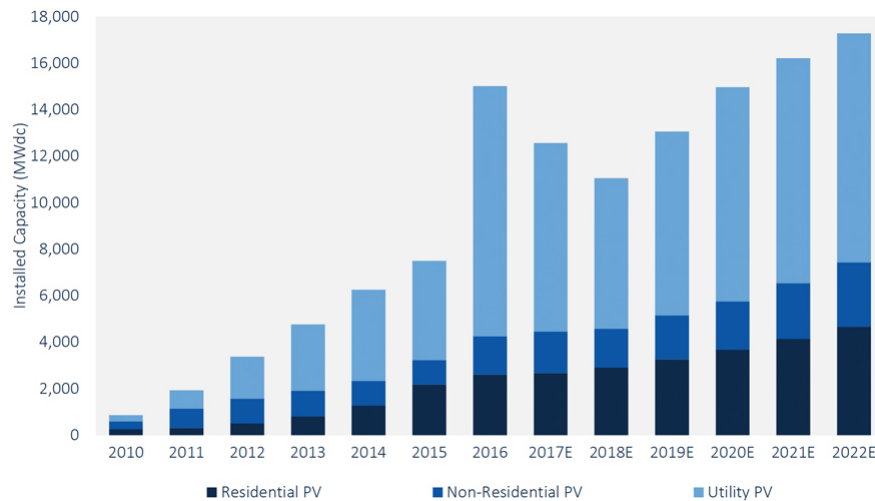


**Figure 1.8:** Installed PV capacity in the U.S. from 2010 until the present. Forecasted (E) values included until 2022. Obtained from [16].

In terms of individual capacity, the installed power in most of the operating plants nowadays is in the order of megawatts [15]. The first installations of this kind were constructed in 2010, and from this point onwards new capacity records have been constantly reported. For instance, despite being one of the larger installations in 2012, the *Agua Caliente Solar Project* (Arizona, 290 MW) was surpassed in a period of just years by the *Topaz* and *Desert Sunlight* solar farms (California, 550 MW). These were followed by the *Longyangxia Dam Solar Park* (Qinghai, 850 MW) in 2016 and by the two largest LSVP installations nowadays: the *Kurnool Solar Park* in India and the *Yanchi Solar* station in China; both with a installed power of 1000 MW.

The increasing number of large scale installations has been mainly driven by an important reduction in the associated costs [17]. This is in part due to the lower cost of solar modules on account of technological improvements and lower-priced alternatives manufactured in China. But also, the prices of inverters and other services (such as sales, permitting inspection, connection to the grid, etc.) went significantly down as a retroactive consequence of the scaling process.

In spite of these advantages, there are still some obstacles that can hinder the design and construction of large PV plants. To this regard, one of the most critical factors is the land utilization. Indeed, in order to produce enough electricity and thus make a system economically viable, several acres of land are often required. This not only results on a negative environmental impact but also implies an additional cost due to land acquisition and installation of transmission lines.

In order to mitigate this effect, most large scale PV plants keep relying on crystalline silicon technology. As commented in the previous paragraph, this is also a consequence of lower module prices but, more importantly, of the higher efficiency of c-Si compared to the alternatives. This means that more energy can be yield per unit of area, leading to a significant reduction in the use of land.

### 1.3.2 Operational aspects on LSPV

The performance of a photovoltaic module during normal operation is remarkably lower than under standard test conditions (STC) measurements [6]. The main reason behind this is the effect of meteorological conditions, among which irradiance level, ambient temperature and wind speed play a significantly important role.

Despite being directly proportional to the electricity production, high irradiance levels can also cause an increase in the module temperature above the standard 25 °C. This has a marked negative effect over the overall module performance since it leads to a reduction in the open circuit voltage and, consequently, total power output.

In any case, the consequences of this can be more or less important depending on the exact location and time of the year. For this reason, when assessing the influence of meteorological conditions over the performance of a PV module it is always convenient to focus on a specific location and rely on precise weather data collected on site. For instance, in climates such as The Netherlands the average irradiance throughout the year is rather low and windy days are frequent. This makes it possible for modules to cool down naturally and hence become more efficient.

However, as was commented on the previous section, most solar farms are located in locations in which this phenomenon is not likely to happen. A representative example of this is the distribution of solar farms in the United States. Indeed, as illustrated in Figure 1.9, most of the large-scale installations are located in the West side of the country, namely the states of California, Arizona and Nevada.

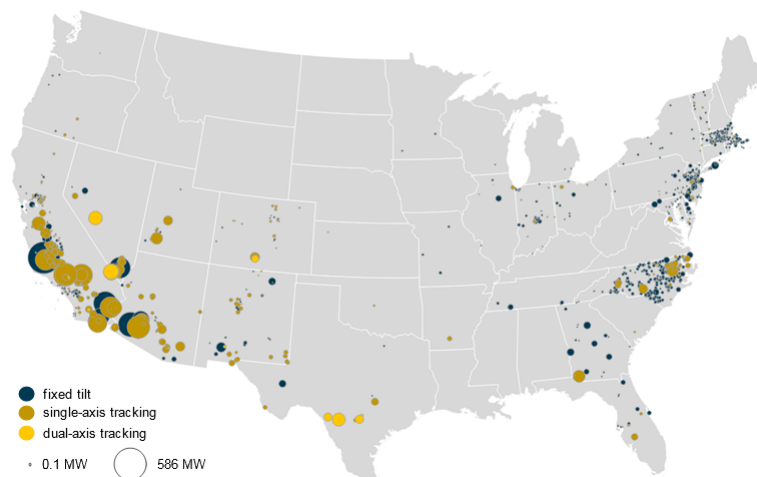


Figure 1.9: Operable utility-scale PV in the United States. Data for 2015. [18]

These locations are well-known for their high levels of irradiance (around or even higher than 7 kWh per square meter and day) and moderate wind speed. Hence, a small decrease in the module's operating temperature may lead to a substantial change in the total energy output of the installation.

## 1.4 Objective and outline of the thesis

Based on the fact that most PV applications nowadays keep relying on crystalline silicon, most of the current research is focused on improving the efficiency of these type of devices. Some remarkable contributions to this field are minimization of optical losses through anti-reflective coatings, light trapping by means of texturing, rear surface reflectors, small-area electrical contacts, etc. [6]

Within this framework, the objective of this project is to improve the performance of crystalline silicon devices by reducing their operating temperature. In particular, a passive approach based on the use of infrared optical filters is proposed.

This thesis is structured in eight main chapters. To begin with, **Chapter 1** has briefly set the motivation of this project. In **Chapter 2**, the main parameters used to describe the performance of solar cells are introduced and the negative effect of temperature over the performance of PV devices is discussed.

Following the theoretical background, **Chapter 3** presents a detailed explanation and subsequent validation of the thermal model. Afterwards, this model is used in **Chapter 4** to define the optimum wavelength range of reflection.

Based on these results, the following sections of the thesis are mainly devoted to the design and construction of an optical filter. First, **Chapter 5** introduces the basis of optics theory and describes the main approaches used for the design of optical filters. Following this, **Chapter 6** and **Chapter 7** are focused on the design and construction of the filter.

Finally, **Chapter 8** summarizes the main conclusions of the project and gives recommendations for further research.



## Chapter 2

# Temperature management in solar cells

The aim of this chapter is to give insight into the negative impact of the operating temperature over the performance of a PV module. For this purpose, the electrical parameters of solar cells are firstly defined. Afterwards, the relationship between operating temperature and open circuit voltage is described. Finally, some approaches to tackle the negative impact of temperature are presented.

### 2.1 Electrical parameters of solar cells

The objective of this section is to introduce the parameters used to characterize the performance of solar cells. Generally, these can be reduced to the *peak power* ( $P_{\max.}$ ), *short circuit current density* ( $J_{sc}$ ), *open circuit voltage* ( $V_{oc}$ ) and *fill factor* (FF). This knowledge will be used afterwards to explain the negative effect of temperature over the performance of a solar cell.

- **Short circuit current:** the short circuit current is the current that flows through the external circuit when the contacts of the solar cell are short circuited [6]. This parameter depends both on the incident irradiance and on the area of the solar cell. Often, the *short circuit current density* is used instead in order to remove the dependence on the cell area. This allows the comparison between solar cells with different geometries.
- **Open circuit voltage:** the open circuit voltage is the maximum voltage that can be delivered by a solar cell when no current flows through the external circuit [6]. It corresponds to the point at which the dark current (no illumination) compensates the photo current.
- **Fill factor:** the fill factor is the ratio between the maximum power produced by a solar cell and the product of  $V_{oc}$  and  $I_{sc}$ , as indicated in Equation 2.1 [6]. This

parameter is normally used to assess the quality of a solar cell: the higher the fill factor, the better.

$$FF = \frac{P_{max.}}{J_{sc} V_{oc}} = \frac{J_{mpp} V_{mpp}}{J_{sc} V_{oc}} \quad (2.1)$$

- **Conversion efficiency:** the conversion efficiency is perhaps the most relevant parameter of a solar cell, since it determines the maximum power that a solar cell can deliver at a given incident radiation. Typically, the incident irradiance of the AM 1.5 G spectrum ( $P_{in} = 1000 \text{ W m}^{-2}$ ) is taken as a reference, enabling the comparison between different types of solar cells.

$$\eta = \frac{P_{max}}{P_{in}} = \frac{J_{mpp} V_{mpp}}{P_{in}} = \frac{J_{sc} V_{oc} FF}{P_{in}} \quad (2.2)$$

## 2.2 Influence of temperature on PV module performance

As discussed in the previous chapter, an increase in the operating temperature above the standard  $25^\circ\text{C}$  can hamper the electrical performance of PV devices.

From Figure 2.1 (solid red line) it can be seen that this is mainly a consequence of a lower open circuit voltage. Indeed, even though the short circuit current increases subtly with the temperature, its effect does not compensate for the aforementioned losses [6].

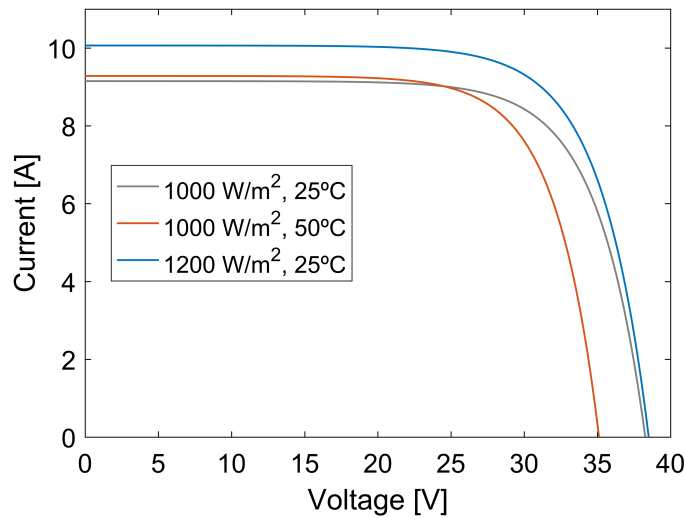


Figure 2.1: Effect of temperature and incident irradiance on the I-V curve of a solar cell.

From a mathematical point of view, the effect of temperature over the performance of a solar module is represented by a parameter known as *thermal coefficient* [6]. This can be individually defined for the open circuit voltage, short circuit current and maximum power output. These three parameters are normally used for characterize the performance of solar cells and thus are included in the module's technical datasheet.

For the open circuit voltage, the thermal coefficient corresponds to the derivative term in Equation 2.3, in which  $T_M$  is the operating temperature of the module.

$$V_{oc}(T_M, G_{STC}) = V_{oc}(STC) + \frac{\partial V_{oc}}{\partial T}(STC)(T_M - 25^\circ C) \quad (2.3)$$

This formula estimates the variation in  $V_{oc}$  due to the operating temperature only. Therefore, the incident irradiance is assumed to be constant and equal to the standard ( $G_{STC}$ ):  $1000 \text{ W m}^{-2}$ . Similar expressions can be written for the short circuit current and maximum power output using their respective thermal coefficients. The main difference in this case is the sign of the thermal coefficient. For the open circuit voltage this term is always negative and hence has a more pronounced effect as the difference between the operating and standard temperature ( $T_M$  and  $T_{STC}$ ) increases.

Under normal operating conditions, the incident irradiance is not constant but rather varies throughout the day. Keeping the temperature constant, the effect of irradiance over the open circuit voltage can be expressed according to Equation 2.4. As can be seen, an increase in the incident irradiance causes the open circuit voltage of a cell to rise.

$$V_{oc}(25^\circ C, G_M) = V_{oc}(STC) + \frac{n k_B T}{q} \ln\left(\frac{G_M}{G_{STC}}\right) \quad (2.4)$$

However, this effect is not particularly pronounced due to the logarithm relationship between the open circuit voltage and incident irradiance. Also, it should be noted that the operating temperature is likely to increase with the irradiance, leading ultimately to a reduction in the open circuit voltage.

The parameter that changes the most with the irradiance is the short circuit current, as can be seen from Equation 2.5 and the solid blue line in Figure 2.1. This is because more incident photons can be effectively excite an electron from the valence band to the conduction band.

$$I_{sc}(25^\circ C, G_M) = I_{sc}(STC) \frac{G_M}{G_{STC}} \quad (2.5)$$

Based on this, the conversion efficiency (Equation 2.2) during normal operation can either increase or decrease throughout the day. Generally, this depends on whether the possitive impact of irradiance compensates for the negative consequences of a high operating temperature.

This situation is different when only the infrared radiation is considered. In this case, Equation 2.5 does not apply since the energy of infrared photons is lower than the band gap of the cell. However, infrared light can be effectively absorbed in other layers of the module and ultimately elevate their temperature during operation.

As a result, the open circuit voltage would significantly decrease while the short circuit current would remain the same. Hence, a progressive decrease in the overall module efficiency can be expected as more light beyond the band gap is absorbed.

## 2.3 State-of-the-art

Different approaches have been presented in order to tackle the negative effect of temperature over the performance of photovoltaic modules. Most of them, however, involve active systems in which the excess of heat is forcibly removed by means of an additional fluid. A representative example of this is the case of hybrid photovoltaic-thermal collectors (often abbreviated as PVT) [19].

This type of systems are able to extract most of the heat generated in the solar module by means of a supportive medium. In the majority of PVT collectors, this is done by integrating a water circuit to the PV module, as depicted in Figure 2.2a. If the water flowing through the external circuit is at a temperature lower than the module, then the excess of heat in the module is transferred to the water by means of convection. This ensures that most of the heat is immediately removed from the cell, hence improving its efficiency. In addition, an advantage of this systems is based on the use of hot water for domestic purposes.

However, there are two main drawbacks that need to be considered. First, the manufacturing process of hybrid modules is rather complicated due to the integration of all the tubes that comprise the water circuit. Besides, this solution is not able to reduce all the heat generated in the cell, but only a fraction of it. This is partly due to limitations in the transport of heat from the module towards the external circuit. In addition, depending on the water temperature, the heat removal might not be sufficient to substantially affect the performance of the module.

A similar solution often used in large scale installations is based on floating PV modules [20]. This implies that the rear side of the module is in contact with water, hence leading to some additional heat transfer. Nevertheless, this approach is not very effective since the removal of heat is limited by the fact that water is still, rather than in movement.

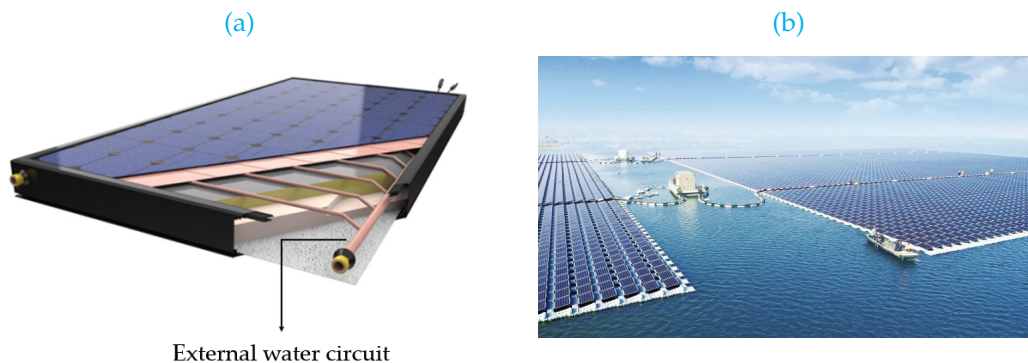


Figure 2.2: Examples of active cooling mechanisms. Obtained from [21, 22] (a) flat PVT collector and (b) floating PV farm (Liulong, China).

Taken this into account, passive heat removal mechanisms are preferable since they do not depend on an additional support. However, the number of publications based on this approach is rather scarce. A significant contribution to this field has been made by A. Raman *et al.* [23]. This is aimed at inducing passive radiative cooling in a heat-absorbing structure under direct sunlight. Even though the focus of this study is not

put on PV devices, the idea developed can be extrapolated to this particular case.

Basically, this research line is based on the use of a photonic radiative cooler. The objective of this system is to significantly reduce the absorption of light (thus enhancing the reflection in the interface) while maximizing the heat radiated at the surface. This is done to guarantee that the heat radiated by an object back to the space is higher than the heat gained via light absorption and thermal radiation from the surroundings. Under these circumstances, it was proven that the object of a heat-absorbing material could be reduced in around 5 °C.

Just recently, the possibility of extrapolating the aforementioned idea to the field of photovoltaics have been considered [24]. That is, using a photonic approach to passively reduce the operating temperature in PV devices. At the moment, this is the closest approximation to the scope of this thesis. In fact, both research lines are based on developing a structure able to efficiently absorb light in the band gap of the cell and partially block the infrared component.



## Chapter 3

# Thermal model

The objective of this chapter is to present the thermal model developed at the beginning of the thesis. This tool is particularly important since it enables the determination of the optimum wavelength range of reflection. In addition, it can be used to predict the temperature of a module in which a certain filter has been installed.

Along this chapter the theoretical principles behind the thermal model are firstly introduced. Afterwards, the reference system is described and the heat transfer mechanisms between the system and its surroundings are determined. Finally, these concepts are translated to a model in COMSOL which is validated the end of the chapter.

### 3.1 Heat exchange mechanisms

Whenever there is a difference of temperature in a medium or between media, heat transfer occurs by any of its three forms: conduction, convection and radiation [25]. In the following sections, the physics behind these mechanisms are explained thoroughly. In addition, the main equations used to characterize the heat transfer are developed and the heat transfer coefficients are defined.

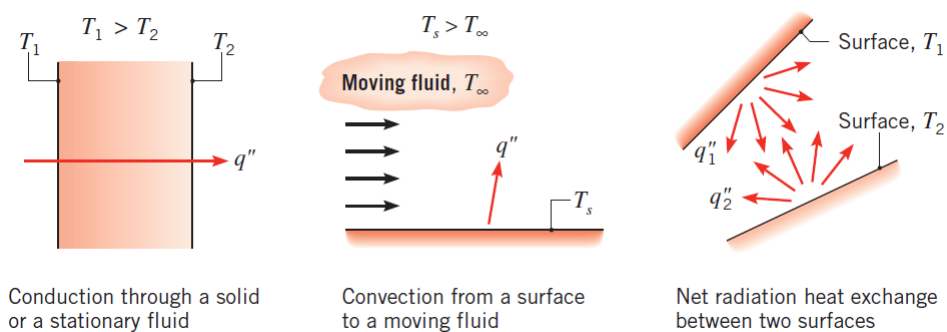


Figure 3.1: Schematic representation of conduction, convection and radiation. Extracted from [25].

### 3.1.1 Conduction

As can be observed in Figure 3.1, conduction is referred to the transport of energy through a medium (which can be either a solid, a liquid or a gas) in which exists a gradient of temperature [25].

This transport of heat can be understood by considering the influence of temperature over the molecular structure of a given medium. In particular, as the temperature increases the energy content of the lattice becomes higher. This gives rise to multiple collisions within the lattice that ultimately cause the molecules to interact with each other. As a consequence, energy is progressively transferred along the structure.

The resulting conductive heat flux can be quantified by means of the *Fourier's law* (Equation 3.1) [26]. In this formula, a negative sign has been included to emphasize that heat is transferred in the direction of decreasing temperature.

$$q_x'' = -\kappa \frac{dT}{dx} \quad (3.1)$$

Similarly to other expressions used in the field of heat transfer,  $q_x''$  ( $W/m^2$ ) is defined as the rate by which heat is transmitted in the  $x$ -direction and through the flux cross sectional area. In the case of conduction, it can be seen that this value is directly proportional to the gradient of temperature (driving force) and the thermal conductivity,  $\kappa$  ( $W/mK$ ). This last parameter is an intrinsic property of the material and gives a measure of thermal resistance. Materials with a low thermal conductivity are more resistant to heat transfer while in materials with a higher  $\kappa$  heat exchange occurs faster.

### 3.1.2 Convection

The main approach used to determine the rate of heat transfer between a surface and an adjacent fluid in motion is the *Newton's law of cooling* [27]. Similarly to Fourier's equation in conduction, this principle states that the convective heat flux is directly proportional to the difference in temperature between the surface and the streaming fluid. That is

$$q_s'' = \propto (T_s - T_\infty) \quad (3.2)$$

in which  $q_s''$  is the surface flux,  $T_s$  the surface temperature and  $T_\infty$  is the fluid temperature away from the surface. If this proportionality is expressed by means of a heat transfer coefficient,  $h$  ( $W/m^2K$ ), the rate of convection can be defined as follows:

$$q_s'' = h(T_s - T_\infty) \quad (3.3)$$

This coefficient has proven to play a major role in convection transfer. Unlike thermal conductivity,  $h$  is not a material property but rather a physical variable that depends

mainly on fluid motion but also on geometry, fluid properties and in some cases, temperature difference.

To begin with, fluid motion can be classified in two different categories:

- *Forced convection.* Fluid motion is caused by external means, such as a fan, a pump or atmospheric winds.
- *Free (natural) convection.* Fluid motion is induced by buoyancy forces, which are due to density differences caused by a temperature variation within the fluid.

Identifying these two forms of convection properly is crucial in order to estimate the heat transfer coefficient. There are multiple correlations available in the literature that allow the calculation of  $h$  in both circumstances. This type of formulas are generally meant to calculate a dimensionless parameter known as Nusselt number (Nu), which expresses the ratio between convective and conductive transfer [6]. Following this, the determination of the convection coefficient is straightforward; only the thermal conductivity of the fluid ( $\kappa_f$ ) and the characteristic length of the solid (L) are needed, as can be seen in Equation 3.4.

$$Nu = \frac{h L}{\kappa_f} \quad (3.4)$$

Down below, a method for calculating the convection coefficient under forced and natural convection is provided. This is a selection of various formulas available in the literature that have proven to be particularly accurate for the case of photovoltaic modules.

### Forced convection

In solar modules under normal operation, forced convection is motivated by the flow of wind around the surface. In order to define a correlation that can be applied to this particular case, different approaches have been compared: either developed from fundamental heat transfer [25] or derived from wind tunnel measurements [28–31] and field measurements [32–34].

The main conclusion obtained from this comparison is that fundamental heat transfer theory leads to the lowest value for the convective heat coefficient. Indeed, a number of reasons have been used to explain why basic heat transfer theory does not fully represent the case of a PV module under normal operation [35]. First of all, it is highly unlikely that the module's upper surface behaves as isothermal, since small scale wind fluctuations cause a gradient of temperature along the surface. Besides, naturally occurring wind contains free stream turbulence resulting from the edges of fences, trees and roofs. These factors are not indicated in the general heat transfer formulae, but are known to enhance convection on the surface.

On the other hand, the correlations extrapolated from field measurements have proven to be slightly more accurate than those obtained from early wind tunnel experiments. The main reason behind this is that the studies made on a wind tunnel did not report the influence of module tilt over heat transfer; which is not very realistic provided that solar panels are normally titled in order to maximize their power output. In terms of heat transfer, when a module is tilted the edges acts as an obstacle to the incoming

wind, which gives rise to flow phenomena such as separation and reattachment. As a result, the flow of air around the module becomes turbulent and more heat is exchanged between the module and its surroundings.

Taking the aforementioned factors into account, it has been found that one of the best approaches to calculate the forced convection coefficient is to use Equation 3.5, in which  $w$  is the wind speed measured in m/s.

$$h_{forced} = 2.56 w + 8.55 \quad (3.5)$$

### Free convection

Natural convection can also represent an important fraction of the heat exchanged between a PV module and its surroundings. Its effect is particularly significant on days with almost no wind—so that forced convection is not the predominant heat transport mechanism—and in cold climates; in which the exchange of heat is mainly motivated by the severe difference between the temperature of the module and the surrounding air.

In this case, the convective heat transfer coefficient is generally obtained from the Nusselt number (Equation 3.4), for which different correlations can be found in literature.

To begin with, free convection at the bottom of an inclined plate can be calculated as follows:

$$\overline{Nu} = \left[ 0.825 + \frac{0.387 Ra^{1/6}}{\left[ 1 + (0.492/Pr)^{9/16} \right]^{8/27}} \right]^2 \quad (3.6)$$

In this formula,  $Ra$  and  $Pr$  are the dimensionless numbers of Rayleigh and Prandtl respectively. Basically, these parameters contain information about the effect of temperature over the physical properties of air as well as about its thermal conductivity.

On the other hand, free convection at the top surface can be calculated by means of Equation 3.7, as long as the following conditions are met:

$$10^5 < Gr Pr \cos\theta < 10^{11}$$

$$15^\circ < \theta < 75^\circ$$

$$\overline{Nu} = 0.14 \left[ (Gr Pr)^{1/3} - (Gr_{cr} Pr)^{1/3} \right] + 0.56 (Gr_{cr} Pr \cos\theta)^{1/4} \quad (3.7)$$

In this formula,  $Gr_{cr}$  is the critical Grashof number, which can be defined as the value at which the Nusselt starts to deviate from laminar behaviour.

Finally, in a situation in which both forced and natural convection occur, it is possible to define an overall convective heat transfer coefficient by means of Equation 3.8 [6, 25].

$$h_T = \sqrt[3]{h_{\text{forced}}^3 + h_{\text{free}}^3} \quad (3.8)$$

### 3.1.3 Radiation

Compared to conduction and convection, thermal radiation is a particularly interesting process since it does not require an intervening medium for it to happen [25]. An illustrative example of this heat exchange mechanism is the case of a hot object placed in a vacuum. In this situation, it is known that the object will eventually cool down, in spite of the absence of wind.

In this case, the hot surface starts to emit radiation as a consequence of its finite temperature, i.e. higher than 0 K. The subsequent transport of heat from the surface to its surroundings can be understood by two different means: either the propagation of the emitted particles (so-called *photons*) or electromagnetic waves.

The total heat emitted by a surface can be derived from the *Stefan-Boltzmann law* of radiation [6, 25]. This general principle states that for an ideal radiator or *blackbody* the total emitted power ( $E_b$ ) can be defined by means of Equation 3.9, in which  $T_s$  is the absolute temperature (K) of the surface and  $\sigma$  is the Stefan-Boltzmann constant.

$$E_b = \sigma T_s^4 \quad (3.9)$$

A blackbody is an idealized type of surface (hence not existing in nature) that absorbs all the radiation that is incident on it; regardless of wavelength and angle of incidence [6]. In this theoretical scenario, the temperature of the blackbody would progressively increase and, consequently, the surface would start to emit radiation. Since energy is emitted in form of electromagnetic waves, the heat flux in this case is generally expressed per unit of area, over all wavelengths and in all directions.

This general principle can be modified in order to obtain the radiative heat flux of a real surface. For this, an additional term called *emissivity* ( $\varepsilon$ ) is introduced, resulting in Equation 3.10. It can be noted that the emissivity gives a measure of how efficiently a surface emits energy compared to a blackbody. It ranges from 0 to 1 and depends strongly on the material and its finish.

$$E = \varepsilon \sigma T_s^4 \quad (3.10)$$

#### Exchange of radiative heat between an object and the atmosphere

A special case in nature involves radiation exchange between a small surface at  $T_s$  and a much larger, isothermal surface that completely surrounds the smaller one [25]. This is the case of a small object surrounded by a mass of atmospheric air. In this case, the net flux of radiative heat from the object's surface can be expressed as the difference

between the thermal energy released due to radiation emission (Equation 3.10) and gained due to radiation absorption.

This last term is the irradiation at the Earth's surface due to atmospheric emission ( $G_{atm.}$ ) and can be expressed according to Equation 3.11. As can be observed, this formula is similar to the general principle with the exception that it is referred to the so-called *effective sky temperature* ( $T_{sky}$ ). This parameter represents the temperature in the far atmosphere and depends strongly on atmospheric and cloudy conditions.

$$G_{atm.} = \sigma T_{sky}^4 \quad (3.11)$$

Therefore, the net radiative heat between an object and the surrounding air can be finally calculated according to Equation 3.12.

$$q''_{rad} = \varepsilon \sigma T_s^4 - G_{atm} = \varepsilon \sigma (T_s^4 - T_{sky}^4) \quad (3.12)$$

### Absorption of radiative heat

Differently than in the previous case, it may happen that radiation is incident on a surface, in which case a different radiative flux called *irradiation* should be considered instead.

Depending on the type of surface, portions of the incident irradiation can be either reflected, absorbed and/or transmitted, as illustrated in Figure 3.2. As can be seen, a surface can either be *opaque* or *semitransparent* to the incident radiation. In the first case, this implies that all the incident light is immediately reflected at the interface air-surface. On the contrary, in a medium is *semitransparent* (Figure 3.2b) a fraction of the incoming irradiance is effectively absorbed while the remaining is either reflected or transmitted. Among the three components, only the fraction absorbed accounts for a source of heat since the rays reflected and transmitted do not even interact with the medium.

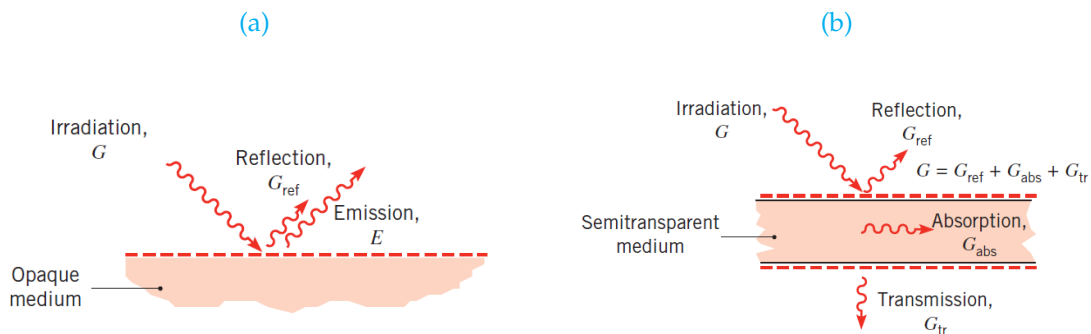


Figure 3.2: Radiation at a surface of two different media. (a) semitransparent medium and (b) opaque medium. Extracted from [25]

Therefore, it can be concluded that in order to determine the heat input of an object exposed to sunlight it is necessary to firstly determine its absorption coefficient. That

is the percentage of the incoming radiation that is effectively absorbed at each wavelength.

## 3.2 Ray tracing

In order to determine the fraction of light absorbed in a PV module, a ray tracing evaluation needs to be firstly done. This enables the calculation of the individual heat sources across the constituent layers of a solar module.

For this purpose, GenPro4 has been used. This software is based on an optical algorithm for multilayer structures developed and validated by Dr. R. Santbergen [19, 36]. This can be used to analyze different solar cells configurations, from crystalline silicon to thin film.

The operating principle of this software is based on elemental optics theory. Further information to this regard is given in Chapter 4. For clarity purposes, the focus of this section is put on defining the solar module configuration used during the ray tracing simulations. This gives more insight into the different heat sources throughout the module.

### 3.2.1 Reference configuration

The structure used as a reference for the optical simulations in GenPro is presented in Figure 3.3. As can be observed, this is a standard crystalline silicon module in which the main elements are glass, encapsulant and a textured c-Si solar cell with alloyed aluminum back contact. Since this last layer is opaque, neither the back EVA nor the *Tedlar* have been modeled optically.

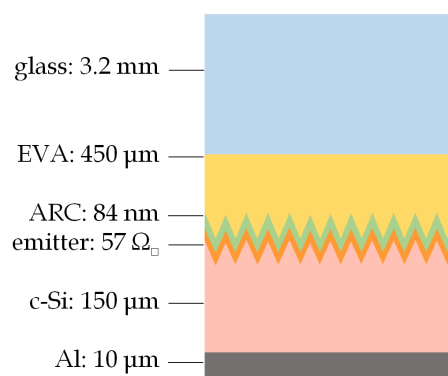


Figure 3.3: Reference solar module configuration for the optical simulations in GenPro4.

With regard to the solar cell, the following elements are considered: anti-reflective coating ( $\text{Si}_3\text{N}_4$ ), emitter and absorber. As can be see, the emitter is defined by means of its sheet resistance rather than by its thickness. This is because even though the thickness

of this layer is normally around 300 nm, only the first nanometers present a level of  $n$ -type doping higher than the bulk doping concentration.

In fact, the *effective emitter thickness* ( $d_e$ ) is defined according to Equation 3.13. Typical emitters have a sheet resistance comprised between 50 and 70  $\Omega_{\square}$ , which corresponds to 70 to 50 nm of effective thickness.

$$d_e = \frac{3.5 \mu\text{m} \Omega_{\square}}{R_{\text{sheet}}} \quad (3.13)$$

That being said, it should be noted that the absorber and emitter have been modeled separately in order to take into account the influence of doping, which has been assumed to be  $1.0 \cdot 10^{16} \text{ cm}^{-3}$  and  $3.3 \cdot 10^{20} \text{ cm}^{-3}$  respectively. Indeed, by adding  $p$  or  $n$ -type doping to a semiconductor free electrons and holes are introduced in the material. These free charge carriers can ultimately absorb part of the incident light leading to a phenomenon known as *free carrier absorption*, which despite not leading to the generation of an electron-hole pair is likely to have a significant impact over the module's temperature.

Last, it should be noted that this configuration does not include the metal front contact. In a standard H-pattern grid (parallel fingers connected by two or three busbars) this represents around an 8.0% of the total area, which implies that the active area of the cell is the remaining 92%. Therefore, it may happen that part of the incident light is either absorbed or reflected in the silver contacts. In order to take this into account, the overall absorption of the cell ( $A_{\text{cell}}$ ) has been recalculated according to Equation 3.14 [19]. As can be observed, this is a weighted average between the absorption in the active area (ac) and in the metal grid (gr).

$$A = a_{ac}A_{ac} + a_{gr}A_{gr} \quad (3.14)$$

In this formula,  $a$  denotes the fraction of the surface occupied while  $A$  is the absorption factor. For the particular case of screen printed silver, it has been found that  $A_{gr} = 22.7\%$ . After doing these calculations, the effective absorption in each layer has been in approximately a 6%.

### 3.3 Implementation

Following the theory about heat exchange and ray tracing, the objective of this section is to give further insight on how these two elements are integrated on the final thermal model. For this purpose, this section is subdivided in the following parts: overview of the simulations process, geometry definition and selection of materials and, finally, flows of information between the main units.

### 3.3.1 Overview

For reasons of simplicity, the thermal model has been built and evaluated in COMSOL Multiphysics. The main feature of this software is the easy integration of all the heat transfer mechanisms (internal and external) present during the normal operation of a solar module. Furthermore, its extensive material library makes it particularly suitable for defining all the constituent layers.

The operating principle of COMSOL is based on the *Finite Element Method* (FEM). This numerical approach is widely used in different engineering applications, such as heat transfer or fluid dynamics. These systems are defined by means of complex differential equations and hence cannot be analytically solved for the majority of geometries. As an alternative to this, the FEM is based on subdividing the entire geometry into smaller parts and for each of them solve an approximate form of the complex equation. Hence is evident that the higher the number of elements is, the lower the margin of error in the calculations.

The main units and flows of information within the thermal model are depicted in Figure 3.4. As can be observed, the core part of this diagram is the heat transfer unit defined in COMSOL, which is coupled to the ray tracing analysis carried out in GenPro. On the other hand, the remaining inputs are basically related to meteorological parameters such as temperature and wind speed. All these parameters are evaluated in parallel to calculate the gradient of temperatures throughout the module, which constitutes the output of the simulations.

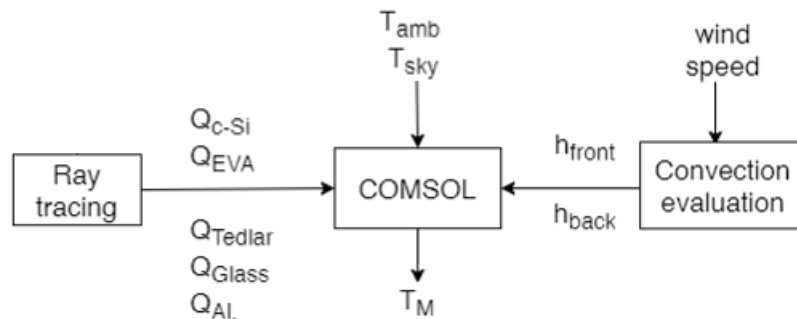


Figure 3.4: Flow chart of the thermal model.

### 3.3.2 Model definition

The development of a model in COMSOL is generally comprised of three different phases. First of all, the geometry is defined and an adequate mesh is generated. This is followed by the selection of materials and definition of any specific property that may be needed. Finally, all the participating physics are integrated and the boundary conditions are set.

## Geometry definition and selection of materials

To begin with, the geometry has been built using the CAD interface of COMSOL. This tool is particularly interesting since it guarantees a complete overlap between all the layers involved. This is an important consideration toward the mesh generation, since empty spaces along the geometry may lead to errors in this part and consequently affect the subsequent simulations.

With regard to the geometry parameters, the work reported in references [37] and [38] has been taken as a guideline and a similar module has been recreated. These studies are also aimed at evaluating the temperature distribution in conventional PV modules. For this purpose, it was found that a mini-module configuration based on a single cell yields a sufficiently accurate result without compromising the computational time.

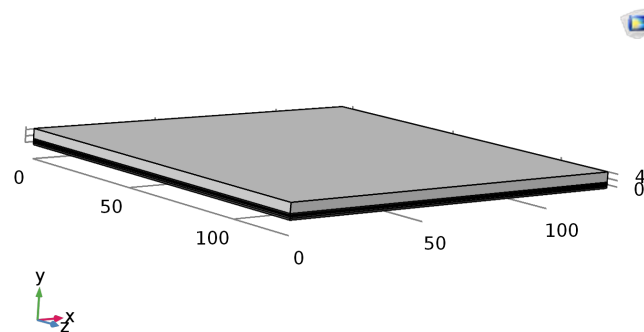


Figure 3.5: Mini-module configuration simulated in COMSOL.

The resulting geometry is depicted in Figure 3.5. As can be seen, this is a 3-D multilayer structure with 12.5 cm side. Similar to standard devices, this configuration includes the following elements: low iron glass (3.2 mm), two encapsulant sheets (450  $\mu\text{m}$ ) and a rear layer made of Tedlar (500  $\mu\text{m}$ ). These can be more clearly seen in the detail view presented in Figure 3.6.

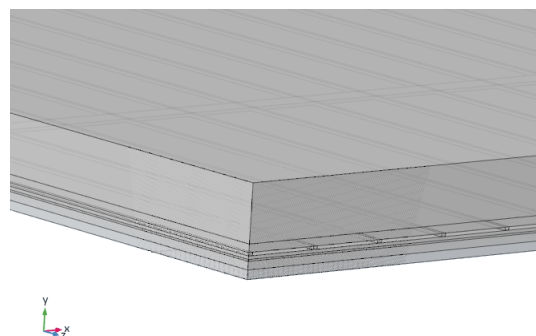


Figure 3.6: Detail of the geometry built in COMSOL. The transparency effect reveals the presence of busbars and fingers.

In order to confirm that a real module can be approximated by a mini-module configuration, a time dependency study was firstly done. For this purpose, the geometry of the

SunPower E19 PV module was taken as a reference. The results from this simulation are depicted in Figure 3.7. As can be seen, the operating temperature increases sharply at the beginning until it reaches the stationary state in less than a hour. This can be more clearly seen in the detail from Figure 3.7b, which reveals that after around 20 minutes the operating temperature stabilizes.

Based on this result, it can be concluded that for heat transfer evaluations a mini-module configuration can be used instead. This is particularly true considering that even meteorological data is frequently given at time steps of one hour. Hence, it can be assumed that from one moment to the other the module reaches rapidly the stationary state.

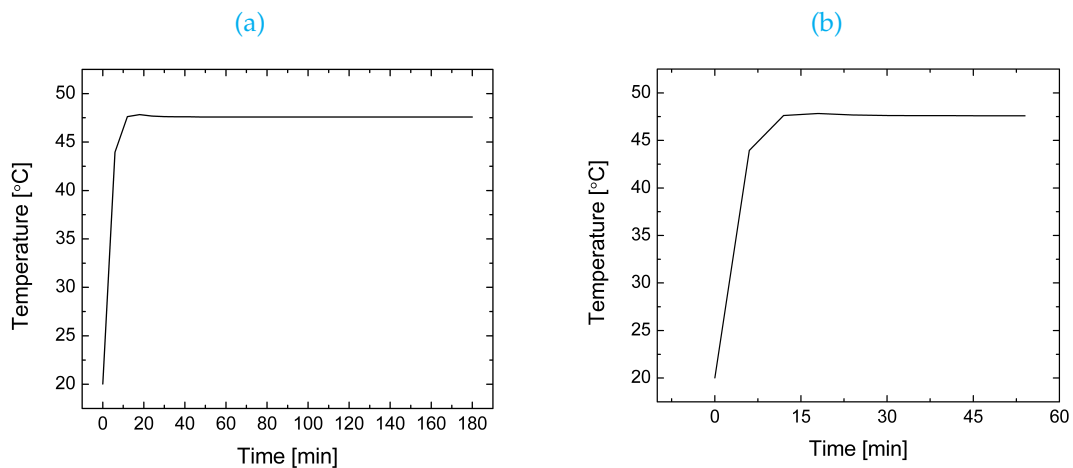


Figure 3.7: Time dependency evaluation in a standard PV module. (a) overall variation and (b) detail.

As for the solar cell, a similar configuration as the one used for the ray tracing study (Figure 3.3) has been built. This is, a  $p$ -type silicon layer with  $n$ -type doping at the front (same doping levels as considered in the ray tracing evaluation). In addition to this, a thin aluminum contact has been modeled at the back. The main difference con respect to the reference configuration used in GenPro lies on the fact that the anti-reflective coating has not been explicitly included, but rather its heat source has been added to the silicon bulk. This is due to the fact that the resistance to heat conduction of thin film is negligible.

In addition to this, a silver front contact has been initially added to the cell. As depicted in Figure 3.8, this is comprised of two busbars and 30 fingers; placed 3 mm apart from each other. In terms of size, the busbars are 1.5 mm wide while the fingers are 250  $\mu\text{m}$  wide. In both cases, the thickness was kept as 18  $\mu\text{m}$ . This was done in order to verify that the silver grid does not account for a significant resistance to the thermal conduction. Also, this structure could be used in case the Joule effect was to be studied more in detail.

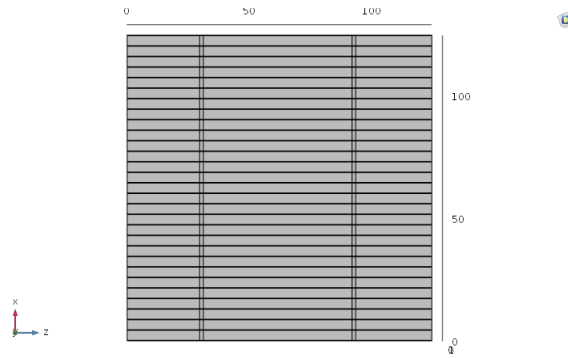


Figure 3.8: Silver front metallization. Conventional H-pattern grid comprised of 2 busbars and 30 fingers.

On the other hand, the material properties required for the thermal simulations are thermal conductivity ( $\kappa$ ), density ( $\rho$ ) and heat capacity ( $C_p$ ) of all the constituent layers. Also, the emissivities ( $\epsilon$ ) of both the front and back surface needs to be included in order to compute the loss of heat due to radiation. The specific values used for the simulations are compiled in Table 3.1. These data has been partially obtained from the COMSOL material library and literature [35, 38].

Table 3.1: Physical parameters used for the thermal simulation.

Material	Thermal conductivity $\kappa$ [W m <sup>-1</sup> K <sup>-1</sup> ]	Density $\rho$ kg m <sup>-3</sup>	Heat capacity $C_p$ J kg <sup>-1</sup> K <sup>-1</sup>	Surface emissivity $\epsilon$
Glass	1.8	2700	750	0.84
EVA	0.32	960	2090	-
Silver	429	10,500	235	-
PV cells	149	2300	838	-
Aluminum	237	2700	900	-
Tedlar	0.56	1370	1760	0.89

### Generation of the mesh

Once the geometry has been built, the mesh can be designed. For this purpose, different configurations can be chosen in COMSOL, from coarse to extremely fine. In this particular case it was found that a regular 'normal' mesh is sufficiently accurate without compromising the computational time. A detail of this configuration is presented in Figure 3.9

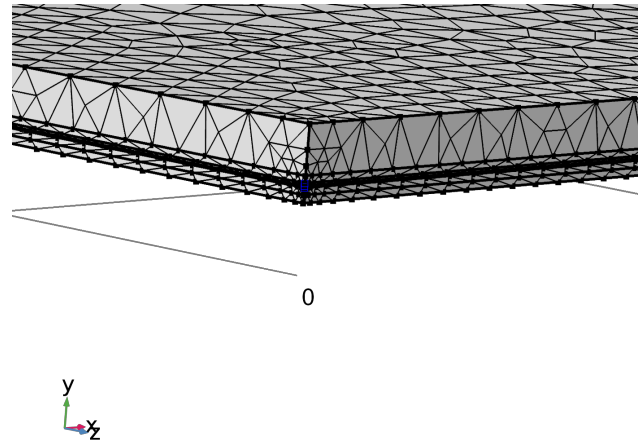


Figure 3.9: Normal size mesh generated in COMSOL.

### Physics implementation: fluid dynamic model

Following the geometry and mesh generation, the last step towards the model construction is the definition of all the physics involved. This also includes setting all the boundary conditions required for the system to be solved.

This step can be more clearly understood by previously defining and correlating all the heat transfer mechanisms involved. This implies doing an energy balance to the system, which is often referred to as a *fluid-dynamic model*. Down below, an overview of this procedure is presented. Please note that most of these concepts are based on the heat transfer theory introduced in Section 3.1. For further information, please consult references [6] and [39].

Taking the diagram depicted in Figure 3.10 as a reference, it can be observed that the Sun irradiation ( $q_{sun}$ ) is the only flux of heat directed towards the module. However, as previously discussed, not all of this incident radiation is an energy input, but rather the fraction of it that is effectively absorbed throughout the module. Denoting  $\alpha$  as the overall absorption, the energy input can be hence defined as:  $\alpha G_M$ .

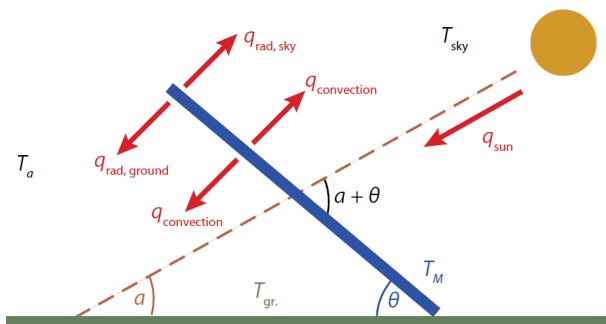


Figure 3.10: Heat exchange mechanisms around a photovoltaic module. Adapted from [6].

Following the absorption of radiative heat, the temperature of the different layers starts to increase steadily due to the internal transport of heat via conduction. In addition to

this, it is important to point out that a fraction of the total heating occurs by means of the *Joule effect*. This is a well-known phenomenon that can be described as the generation of heat due to the flow of electric current through a conductor material. However, it can be proven that its impact over the final module's temperature is negligible compared to the absorption and conduction of sunlight.

Finally, as a consequence of the increase in temperature, the module starts to lose heat via emission and convection. As depicted in Figure 3.10, these phenomena can be reduced to the top and back surface of the panel since their surface is significantly larger compared to the borders. To this regard, it is assumed that the ground below the module is at ambient temperature while the sky temperature can be obtained by means of Equation 3.15 [6, 40].

$$T_{\text{sky}} = 0.0552 T_{\text{amb}}^{3/2} \quad (3.15)$$

On the other hand, both natural and forced convection can be identified in the vicinities of the module. Free convection occurs in the top and back surface as a result of a difference of temperature with respect to the surroundings. On the contrary, forced convection can only be assumed on the top surface, since it is the one exposed to a significant wind stream. Therefore, the heat transfer coefficient for the upper surface can be calculated according to Equations 3.6, 3.7 and 3.8, while for the back surface only Equation 3.7 needs to be used.

Considering all the heat fluxes mentioned, the energy balance around a PV module can be expressed according to Equation 3.16.

$$m C_p \frac{dT}{dt} = \underbrace{\alpha G_M}_{\text{input}} - \underbrace{h_T (T_M - T_a)}_{\text{total convection}} - \underbrace{\varepsilon_{\text{back}} \sigma (T_M^4 - T_{\text{gr.}}^4)}_{\text{emission back surface}} - \underbrace{\varepsilon_{\text{top}} \sigma (T_M^4 - T_{\text{sky}}^4)}_{\text{emission top surface}} \quad (3.16)$$

Each of the elements of this equation can be introduced in COMSOL as boundary conditions within the *heat transfer in solids* package. On the one hand, the incident radiation is individually defined for all the layers by means of a boundary condition. This approach has also been used for defining the loss of heat via radiation and convection in the upper and lower surfaces of the module (four boundary conditions in total). In each of them, the following parameters must be set: heat transfer coefficient and temperature of the ambient, sky or ground; depending on the type of application.

Finally, an additional tool has been added in order to account for the radiation of heat between the intermediate layers. This is term as *surface-to-surface radiation*. Please note that the conduction within the solid does not need to be specifically defined, provided that all the layers have been previously characterized by means of thermal conductivity, heat capacity and density.

### 3.3.3 Heat sources within the module

Provided that each of the constituent layers of a PV module have a different absorption profile throughout the solar spectrum, a convenient approach is to define the individual

heat sources throughout the entire structure [41]. In general, the total radiative heat (in  $\text{W}/\text{m}^2$ ) absorbed by each component can be calculated by means of Equation 3.17, in which  $\lambda_i$  and  $\lambda_f$  are the lower and upper limits of absorption.

$$P_{\text{comp}}^{\text{HS}} = \int_{\lambda_i}^{\lambda_f} A_{\text{comp}}(\lambda) I_{\text{AM1.5g}}(\lambda) d\lambda \quad (3.17)$$

For silicon, however, this formula needs to be adapted since part of the radiation absorbed is converted into electrical power rather than into heat. Therefore, it is necessary to include an additional term that indicates the fraction of the incoming energy that contributes to the heating of the module. Denoting  $E_{\text{ph}}$  and  $E_{\text{gap}}$  as the energy of the incident photons and the band gap of silicon, the following expression can be derived:

$$P_{\text{comp}}^{\text{Si}} = \int_{\lambda_i}^{\lambda_f} A_{\text{Si}}(\lambda) I_{\text{AM1.5g}} \frac{E_{\text{ph}}(\lambda) - E_{\text{gap}}}{E_{\text{ph}}(\lambda)}(\lambda) d\lambda \quad (3.18)$$

Nevertheless, this formula is not realistic since it implies that all the generated charge carriers are effectively collected at the terminals of the cell. If this was the case, the electrical efficiency of the solar cell would be around 48%, which is far from reality. As a matter of fact, the efficiency of standard solar cells has a plateau of around 18-19% in the case of mono-Si and 17-18% for multi c-Si [10].

This is illustrated in the diagrams presented down below. As can be seen, Figure 3.11a represents an ideal scenario in which most of the visible light accounts for electricity production in the cell (area in yellow). On the contrary, Figure 3.11b depicts the electrical power (grey area) of a 17% solar cell. The difference between both curves is therefore an additional form of heat that needs to be added to the thermalization losses.

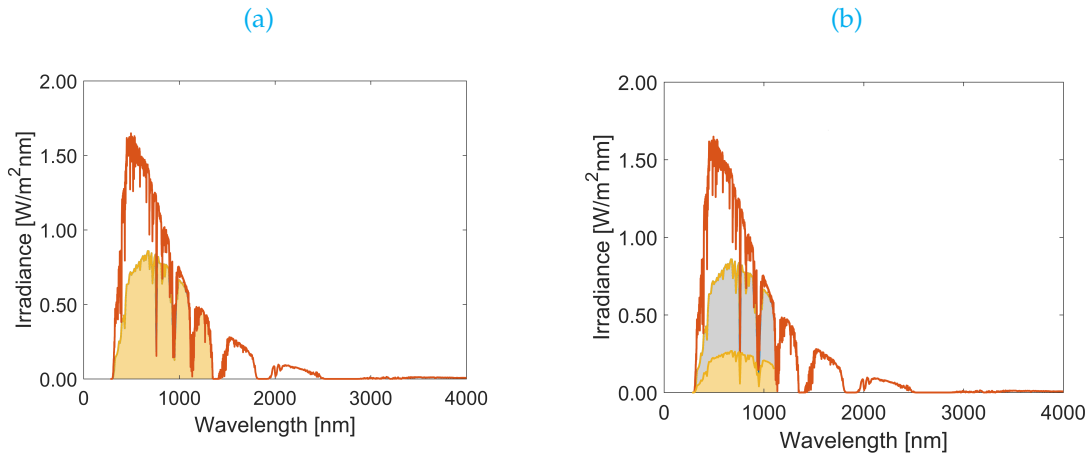


Figure 3.11: Representation of efficiency values. (a) theoretical and (b) real efficiency.

In commercially available solar cells this additional heat accounts for around a 3% of the total spectrum. Based on this, Equation 3.18 can be rewritten as follows:

$$P_{\text{comp}}^{\text{Si}} = \int_{\lambda_i}^{\lambda_f} A_{\text{Si}}(\lambda) I_{\text{AM1.5g}} \frac{E_{\text{ph}}(\lambda) - E_{\text{gap}}}{E_{\text{ph}}(\lambda)}(\lambda) d\lambda + 0.03 I_{\text{AM1.5g}} \quad (3.19)$$

Note that this equation only applies when  $E_{\text{ph}}(\lambda) \geq E_{\text{gap}}$ . Otherwise, the photon does not have enough energy to overcome the band gap of silicon and therefore cannot contribute to the generation of electricity. In this case, the energy absorbed is a direct source of heat and hence Equation 3.17 must be applied instead.

### 3.3.4 Validation

Following the implementation of the thermal model in COMSOL, a study was made in order to validate the model with real temperature data. For this purpose, the field measurements reported in reference [41] have been used. These correspond to a set of meteorological and module temperature data collected in an outdoor testing facility near the city of Cologne (Germany). In all cases, the temperature was measured at the backside of a standard crystalline silicon PV module.

The results obtained from the validation are presented in Figures 3.12a and 3.12b. As can be seen, these plots show the variation of the module temperature as a function of irradiance for three different ambient temperatures: 15, 20 and 25 °C. In each scenario, the wind speed is nearly constant at a value of 0.25 and 4.00 m/s respectively.

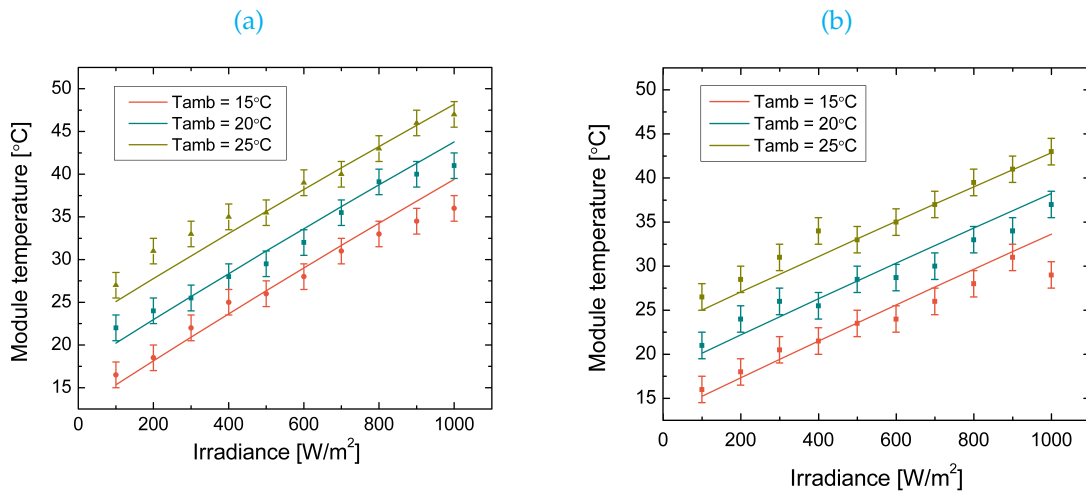


**Figure 3.12:** Comparison of the simulated (lines) and measured (symbols) module temperature for different irradiance levels. (a) wind speed = 0.25 m/s. and (b) wind speed = 4.00 m/s.

In both cases, the results from the COMSOL model are depicted with a solid line, whereas the recorded temperatures are represented by an error mark. The use of the error mark denotes the standard deviation of the measurement and thus reflects the range in which the temperature may fall.

Overall, the results suggest a good agreement between the thermal model and real data. For instance, it can be observed that in both scenarios the module temperature increases linearly with the irradiance, as reported in the literature [6, 39]. Apart from this, the agreement between the simulations and the recorded data is slightly better for the lowest wind speed. In this case, the majority of the simulated values fall within the margin of error of the real temperature.

For the scenario of 4 m/s wind speed the temperature predicted is slightly higher than the recorded values. This is particularly true at higher values of irradiance when the ambient temperature is either 15 or 20 °C. A possible explanation for this may be a lower impact of convection at high wind speeds. However, the trend followed by the measured data indicates an inconsistency at higher irradiances, which may be due to errors in the measurements.



## Chapter 4

# Application of the thermal model

This chapter presents the results obtained during the design of the infrared optical filter. First, the heat sources within the module are defined and the optimum reflectance range is obtained via thermal simulations. Afterwards, different filter structures are explored, taking into account several factors such as performance and manufacturing feasibility (mainly defined by the number of layers and their thicknesses). Finally, the most feasible structures are deposited in the laboratory and the corresponding results are presented.

### 4.1 Definition of heat sources

To begin with, the aim of this section is to define all the heat sources in a standard crystalline silicon module. For this purpose, a ray tracing evaluation was firstly performed in the wavelength range between 280 and 4000 nm. This is based on the reference configuration introduced in Section 3.2.1.

The results obtained from GenPro are depicted in Figure 4.1. As can be seen, the absorption of light in the silicon bulk is dominant at wavelengths lower than the band gap (approximately 1100 nm). From this point onwards, two main areas can be distinguished. The first one goes up to around 2700 nm and is characterized by a predominant absorption in the emitter layer (hence free carrier absorption) and in the aluminum contact. At higher wavelengths, however, the energy of the incident photons is extremely low and hence absorption occurs mainly in the upper glass sheet. This result is in good agreement with similar optical simulations reported in the literature [37, 38, 41]

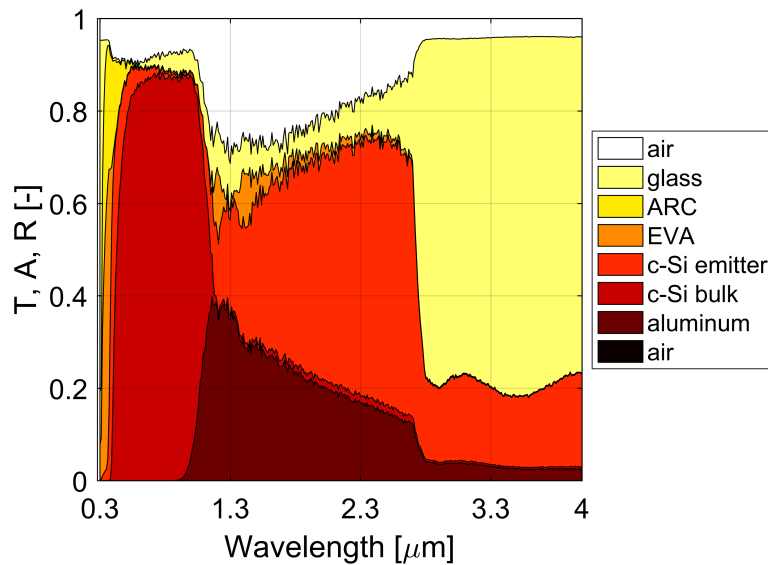


Figure 4.1: Fractions of the solar spectrum transmitted, absorbed and reflected in the constituent layers of a c-Si PV module.

Once the individual absorption coefficients have been determined, it is possible to quantify all the heat sources within a PV module. In order to do this, the spectral heat contributions are firstly calculated at each wavelength by multiplying the absorption of each layer by the incoming radiation. The spectra resulting from these calculations can be seen in Figure 4.2.

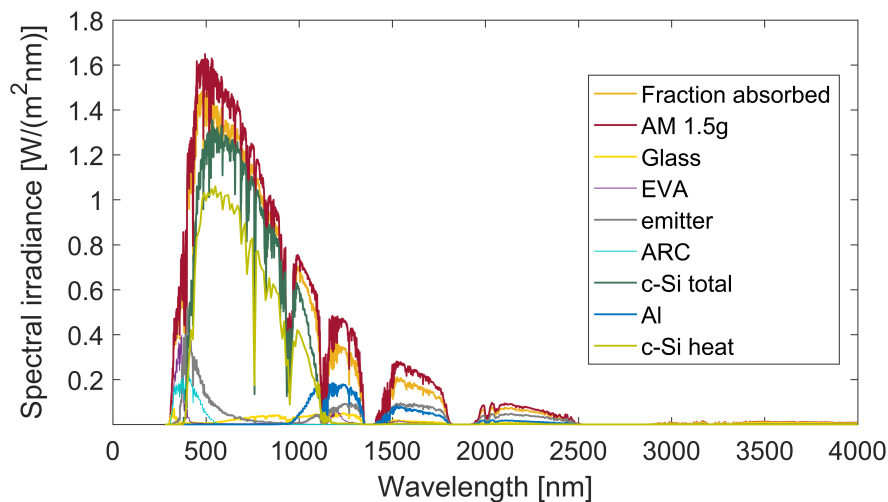


Figure 4.2: Spectral absorption in the constituent layers of a PV module.

As can be observed, it has been assumed that the incident irradiance has the same spectral profile as the standard AM 1.5G. Among the total radiation, it is possible to distinguish the fraction that is effectively absorbed (orange solid line) along with the individual absorption profiles along the module.

It should be noted that for the case of the crystalline silicon bulk, two different curves are included. This is done in order to make a distinction between all the light absorbed

(dark green) and the fraction of light that represents a source of heat (olive green line). In the remaining layers this has not been done, since all the radiation absorbed is a source of heat, as discussed in Chapter 3.

The reason why the absorption profiles have been drawn is to easily calculate the individual heat sources by integrating all the curves. In particular, the diagram presented before allows the calculation of all the heat sources in a simple structure, i.e. without filter on it. If a given filter was to be tested, it would be necessary to recalculate the absorption profiles and draw the corresponding absorption curves.

## 4.2 Optimum wavelength range

In order to determine the optimum wavelength range of reflection, the module temperature is evaluated as a function of the cumulative wavelength. This parameter represents the upper limit of absorption and covers the entire solar spectrum: from 280 (no absorption) to 4000 nm (absorption of all incident sunlight).

More specifically, the cumulative wavelength is increased in steps of 10 nm and for each case the module temperature is simulated. This is done by progressively integrating the individual absorption curves (Figure 4.2) in the range between 280 nm and the cumulative wavelength. As a result, it is possible to estimate the change in module temperature due to the progressive absorption of light, as illustrated in Figure 4.3.

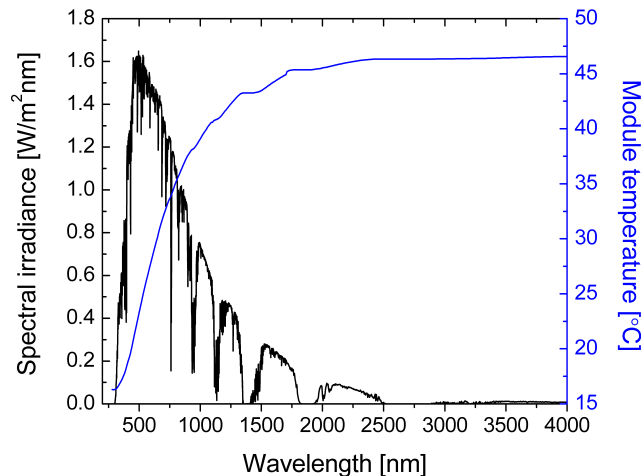
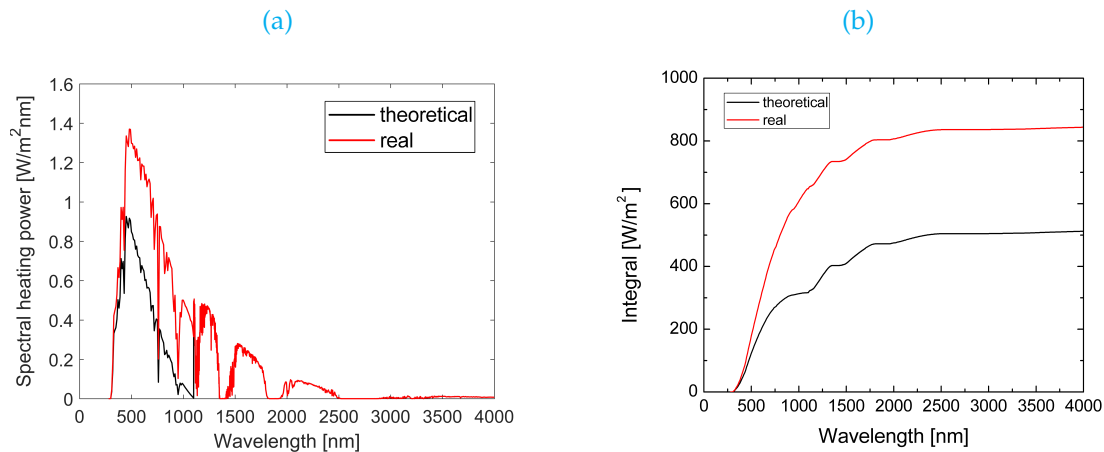


Figure 4.3: Increase in the module temperature due to light absorption along the solar spectrum.

Figure 4.4 shows the result of the integration, as well as the total heating power. As can be observed, two different cases are represented. The first corresponds to an ideal scenario in which all the generated electron-hole pairs are successfully harvested. On the contrary, the second case is more realistic, since an electrical efficiency of 17% is assumed. This implies that part of the charge carriers are not effectively collected at the contacts of the cell, thus accounting for a heat source within the module.



**Figure 4.4:** Heat power inputs to the thermal model. Black line: theoretical case. Red line: realistic case ( $\eta_{\text{cell}} = 17\%$ ) (a) spectral heat power and (b) result from the integration.

As can be seen, the total heating power is considerably higher in a real scenario, as illustrated in Figure 4.4a. Consequently, its integration along all the cumulative wavelength range is also higher (Figure 4.4b). It is important to remark that this is due to the difference between both curves at wavelengths lower than 1100 nm. From this point onwards, both curves become the same, since all the incident irradiance is a source of heat.

Considering the significant difference between both scenarios, it is convenient to base the simulations in a real case. Hence, the cell efficiency has assumed to be 17%. For this case, the temperature profile depicted in Figure 4.7a has been obtained.

As can be seen, an increase in the cumulative wavelength causes the module temperature to rise steadily. This effect is more pronounced at wavelengths lower than 1500 nm. Then it smooths out until it stabilizes at around 2500 - 3000 nm. Based on this, it can be concluded that the optimum range of reflection is comprised between 1100 (band gap of silicon) and 2500 nm. In fact, extending this upper limit further would not be an optimum solution, since it would lead to a more complex and difficult to manufacture filter. On the other hand, just by effectively blocking all the incoming light within 1100 and 2500 nm, the module could be reduced by around  $5^\circ\text{C}$ . This can be clearly seen in the detail from Figure 4.7b.

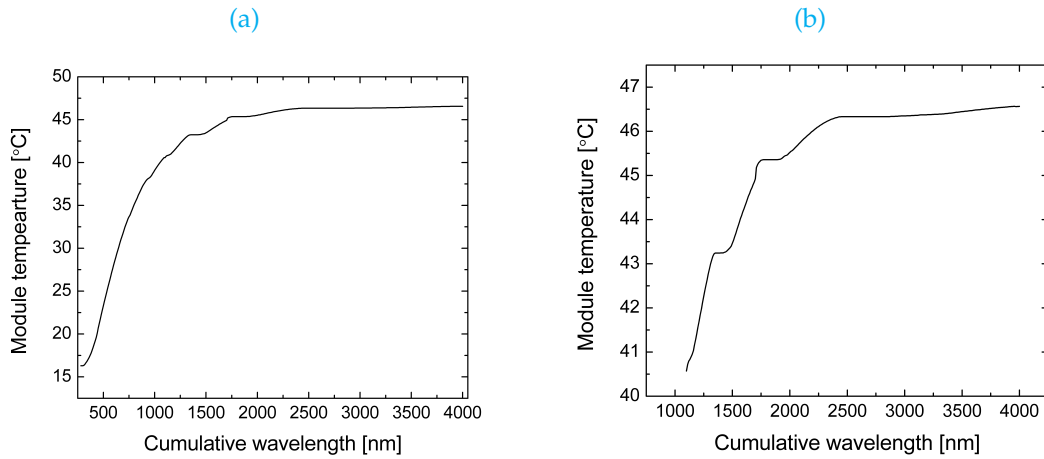


Figure 4.5: Module temperature as a function of the cumulative wavelength (i.e. maximum limit of absorption). (a) general trend (280 - 4000 nm) and (b) detail (1100 - 4000 nm).

### 4.3 Potential benefit

Once the optimum wavelength range of reflection has been determined, the objective of this section is to quantify the impact of an ideal filter (i.e. able to block all light between 1100 and 2500 nm) in terms of annual performance.

As discussed in Chapter 1, this study is ultimately focused on large scale PV installations. This is due to the fact that the repercussion of any possible improvement is considerably higher in these facilities compared to residential installations.

Along this study, the following meteorological factors have been considered: irradiance (global, direct and diffuse), ambient temperature and wind speed. All these components were retrieved from Meteonorm [42]. For the subsequent calculations, the guidelines for PV systems evaluation given by Smets *et al.* [6] have been followed. The main difference lies on the fact that the module temperature is obtained via thermal simulations rather than using a linear correlation. In addition, it should be noted that the efficiency of the inverter, power point tracker and *others* (cabling, soiling, etc.) has assumed to be constant and equal to 0.976, 0.98 and 0.97 respectively.

In order to assess the impact of an IR filter, both mono and poly-crystalline silicon PV modules have been evaluated. In particular, the following modules have been considered throughout this study: Jinko Solar JKM320PP-72 and Trina Solar Honey<sup>M</sup> plus.

To begin with, the case study presented in the *Dutch PV portal* was initially taken as a reference [43]. This hypothetical installation has a capacity of 6.9 MW and is located the south of The Netherlands. Using meteorological data from Rotterdam, it is possible to define the optimum module tilt and orientation according to the procedure described in reference [6]. For this specific combination, the results presented in Table 4.1 have been obtained.

As can be seen, the overall contribution of an infrared filter in this case is rather low (always lower than 1% in terms of energy yield). In particular, it can be seen that the mono crystalline module is less affected by the filter. This can be explained based on its

slightly lower thermal coefficient for open circuit voltage:  $-0.29$  versus  $-0.30$  %/K.

**Table 4.1:** Effect of an infrared optical filter in a PV system in Rotterdam (The Netherlands).

<b>Jinko Poly</b>			
	No filter	Perfect filter	Improvement [%]
Average $T_M$ [°C]	12.44	11.89	4.36
Average $\eta$ [%]	8.55	8.58	0.35
EY $10^6$ [kWh/year]	4.85	4.89	0.74
<b>Trina Mono</b>			
	No filter	Perfect filter	Improvement [%]
Average $T_M$ [°C]	12.44	11.89	4.36
Average $\eta$ [%]	10.70	10.74	0.37
EY $10^6$ [kWh/year]	5.09	5.13	0.72

Nonetheless, it can be concluded that the main reason why the filter does not contribute significantly to the system performance is based on a small variation in the module's operating temperature. Indeed, only in the warmer months of the year a reduction of nearly  $2$  °C was observed, as illustrated in Figure 4.6. These graphical representations show the hourly module temperature throughout a representative day (in terms of incident irradiance and wind speed) in the months of January and August.

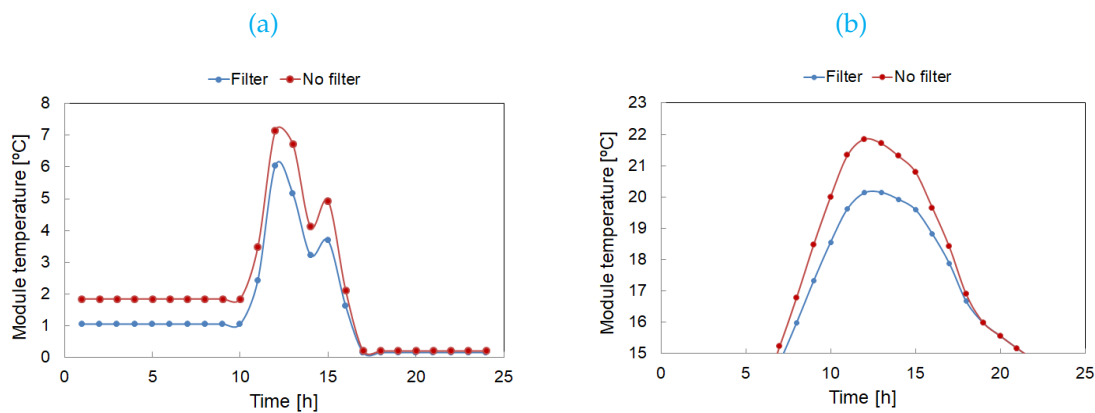


**Figure 4.6:** Module temperature in two representative days in Rotterdam (The Netherlands). (a) January and (b) August.

Therefore, the main reason why the filter contribution is so low is based on climate characteristics. In fact, the ambient temperature in Rotterdam rarely exceeds  $22$  °C, which causes the module to be at a lower temperature. In addition to this, the wind speed is often higher than  $4$  m/s, which ultimately enhances the convection heat transfer from the module to its surroundings. This implies that not only the module is at a low temperature but also that it easily loses heat. Hence, the module cools down naturally and the impact of the filter is low.

Based on this result, the focus of this study was switched to warmer locations. For instance, it was observed that in Palermo (Italy) the module temperature can decrease

by approximately 3 °C in the winter and around 5 °C in the summer, as illustrated in Figure 4.7.

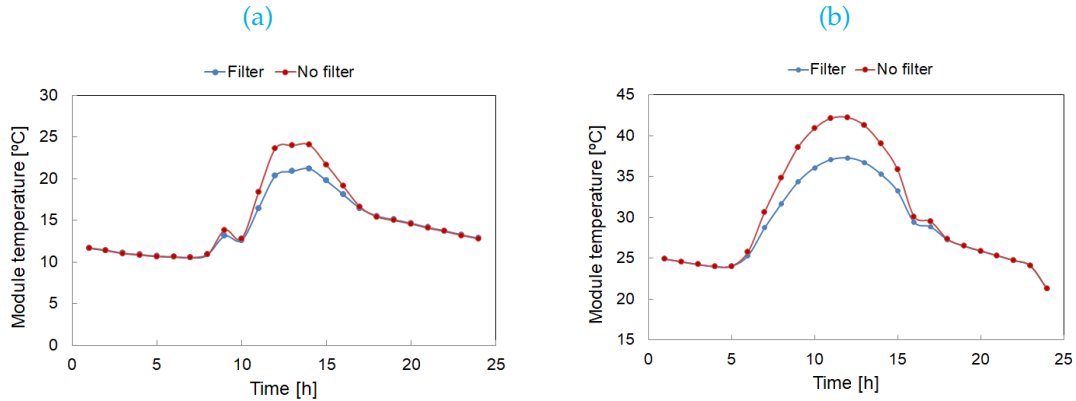


Figure 4.7: Module temperature in two representative days in Palermo (Italy). (a) January and (b) August.

As a consequence, the overall improvement over the system performance is remarkable higher than in the previous case (Table 4.2). In the best scenario, this could lead to an increase of 1.74% in the energy production.

Table 4.2: Effect of an infrared optical filter in a PV system in Palermo (Italy).

<b>Jinko Poly</b>			
	No filter	Perfect filter	Improvement [%]
Average $T_M$ [°C]	23.56	22.12	6.12
Average $\eta$ [%]	8.07	8.17	1.14
EY $10^6$ [kWh/year]	12.80	13.03	1.74
<b>Trina Mono</b>			
	No filter	Perfect filter	Improvement [%]
Average $T_M$ [°C]	23.56	22.12	6.12
Average $\eta$ [%]	10.42	10.54	1.11
EY $10^6$ [kWh/year]	13.46	13.68	1.69

Motivated by this improvement additional locations were studied, namely Tucson (AZ, United States) and Barrancabermeja (Colombia). This were chosen based on the high irradiance levels and, in the case of Barrancabermeja, severe meteorological conditions (around 35 °C average ambient temperature and around 2 m/s wind speed). The results obtained on both cases are gathered in Tables 4.3 and 4.4 respectively.

As can be observed, the improvement in these cases is notably higher. With regard to the change in module's temperature, both locations experience a similar variation, being the change in Barrancabermeja higher due to the low wind speed. As a consequence, the overall energy production is increased up to 1.86% in Tucson and may surpass the 2% in Barrancabermeja.

In the best case scenario, it can be seen that up to 0.31 MWh/year could be gained if an infrared filter was installed. For a 6.9 MW plant in which modules similar than the Jinko (305 Wp) are installed, this would mean that the same production could be achieved using 115 modules less.

**Table 4.3:** Effect of an infrared optical filter in a PV system in Tucson, Arizona (United States).

<b>Jinko Poly</b>			
	No filter	Perfect filter	Improvement [%]
Average $T_M$ [°C]	24.10	22.46	6.81
Average $\eta$ [%]	8.16	8.26	1.27
EY $10^6$ [kWh/year]	14.38	14.65	1.86
<b>Trina Mono</b>			
	No filter	Perfect filter	Improvement [%]
Average $T_M$ [°C]	24.10	22.46	6.81
Average $\eta$ [%]	10.53	10.66	1.12
EY $10^6$ [kWh/year]	15.12	15.39	1.81

**Table 4.4:** Effect of an infrared optical filter in a PV system in Barran-  
cabermeja (Colombia).

<b>Jinko Poly</b>			
	No filter	Perfect filter	Improvement [%]
Average $T_M$ [°C]	29.76	27.72	6.87
Average $\eta$ [%]	7.41	7.57	2.11
EY $10^6$ [kWh/year]	13.49	13.80	2.29
<b>Trina Mono</b>			
	No filter	Perfect filter	Improvement [%]
Average $T_M$ [°C]	29.76	27.72	6.87
Average $\eta$ [%]	9.41	9.55	1.52
EY $10^6$ [kWh/year]	14.63	15.95	2.05

The influence of wind speed and irradiance over the potential increase in the annual energy yield is depicted in Figure 4.8. It should be noted that in all the combinations the ambient temperature was kept constant at a value of 25 °C. This is because this variable does not have an effect as pronounced as irradiance and wind speed. Hence, it was kept constant so that the remaining could be easily compared.

This plot reveals that for average wind speeds higher than 4 m/s, a significant increase in the irradiance needs to occur in order to benefit significantly from the optical filter. On the contrary, at lower wind speeds, the smallest increase in the irradiance can result in energy savings of around 2%.

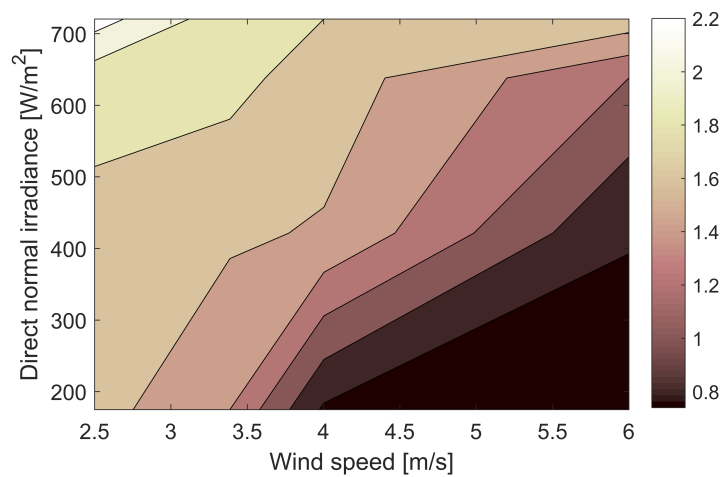


Figure 4.8: Percentage increase in the annual energy yield as a function of average wind speed and direct normal irradiance.



## Chapter 5

# Optical filters

The objective of this chapter is to provide an overview of the different types of optical filters and select the one that is most convenient for this project. Firstly, the theoretical background is introduced. Afterwards, different design rules are presented: from the most classic methods to most complex iterative approaches.

### 5.1 Optics in multilayer structures

To begin with, the aim of this section is to introduce the theoretical principles that define the interaction of light with a multilayer structure. For this purpose, the fundamental concepts and physics laws are firstly introduced. Afterwards, a brief extrapolation is made to the case multilayer structures.

#### 5.1.1 Interaction of light with a medium

From the optical point of view, materials are characterized by their complex refractive index,  $\tilde{n}$ , defined according to Equation 5.1. The real part of this formula is the actual *refractive index* of the material and is related to the speed of light when it travels across it. On the other hand,  $k$  represents the *extinction coefficient* and gives an estimation of how much light does the medium absorb [6].

$$\tilde{n} = n - ik \quad (5.1)$$

As it was previously explained in Section 3.1.3, when light reaches the interface between two optically different mediums, fractions of it are partially reflected and partially refracted, as depicted in Figure 5.1. As can be seen in this diagram, the angle of the scattered light is equal to the incidence angle while for the refracted ray this angle is slightly lower.

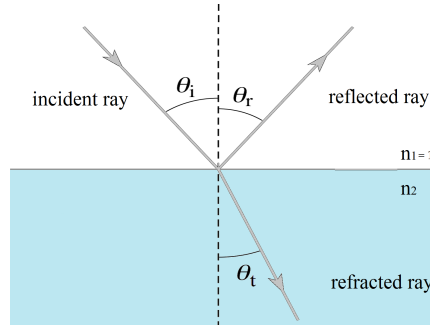


Figure 5.1: Reflected and refracted portions of light at the interface between two media. Adapted from [44].

The fact that  $\theta_i$  and  $\theta_r$  are the same can be derived from *Fermat's principle*, which states that light follows the path of least time [45]. As for  $\theta_t$ , the reason why the refracted ray tends to bend towards the normal (dashed line in Figure 5.1) is because of the change in velocity that it experiences when crosses the interface between air ( $n = 1$ ) and medium 2 ( $n > 1$ ). As a matter of fact, as the refractive index of a given material increases, the speed of light traveling through it decreases and hence  $\theta_t$  becomes lower. Quantitative, this influence can be determined by means of the *Snell's law* (Equation 5.2), which also takes into account the effect of the angle of incidence.

$$n_1 \sin \theta_i = n_2 \sin \theta_t \quad (5.2)$$

In flat interfaces without coating, relations between the incident, reflected and refracted components of light can be derived from the *Fresnel equations*. These calculations are rather tedious and hence have not been included in the present document. Further information about this can be found in Macleod's [46], but for the purpose of this project it is sufficient to know that the following relationship can be obtained for the fraction of light reflected:

$$r = \left| \frac{\eta_1 - \eta_2}{\eta_1 + \eta_2} \right|^2 \quad (5.3)$$

In this formula  $\eta$  represents the modified refractive index, which can be determined according to Equation 5.4 for p and s-polarized light. Please note that sunlight is generally considered to be unpolarized (i.e contains equal amounts of p- and s-polarization) and thus for this case the reflection coefficient is defined as the average value between the two polarizations [6, 19].

$$\eta = \begin{cases} N/\cos\theta & \text{for p - polarized irradiance} \\ N \cos\theta & \text{for s - polarized irradiance} \end{cases} \quad (5.4)$$

For non-absorptive media, all the light that is not reflected is transmitted and hence  $\tau$  can be easily calculated as  $1 - r$ . On the contrary, if light is progressively absorbed in the medium, the intensity of the refracted ray decays exponentially according to the so-called *Lambert-Beer law* (Equation 5.5) [6]. In this formula,  $I_0$  is the initial intensity,  $x$  is the traveled distance and  $\alpha$  is the absorption coefficient. This last parameter is directly

proportional to the imaginary part of the refractive index, as stated in Equation 5.6.

$$I(x) = I_0 e^{-\alpha x} \quad (5.5)$$

$$\alpha = \frac{4\pi k}{\lambda} \quad (5.6)$$

Therefore, for this type of media the transmitted portion of light must be calculated as the incident light minus the sum of the fractions reflected and absorbed.

### 5.1.2 Influence of coatings

The overall reflection of light at a given interface can be significantly modified if a thin coating is present between the two media. Denoting the thickness and refractive index of a film as  $d_c$  and  $n_c$ , the aforementioned situation can be identified whenever the optical thickness of the coating ( $n_c d_c$ ) is smaller than the coherence length of the incident light. In the case of sunlight, such threshold is approximately  $1 \mu\text{m}$  [19].

This phenomenon can be better understood by taking a look at the diagram from Figure 5.2. As can be observed, the addition of a coating between medium 1 and 2 implies that there are two interfaces at which light is reflected. However, since the layer in between is very thin, the rays of light reflected can eventually come across each other's path and hence interfere; resulting in a single reflection ray.

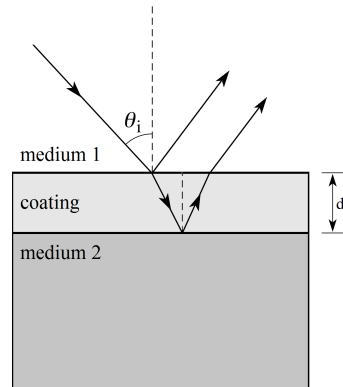


Figure 5.2: Interference effect. Schematic representation of a case of constructive interference.

Considering that light behaves partially as a wave, the magnitude of this ray depends on the phase difference between the original waves. In fact, as illustrated in Figure 5.3, when the peaks of the waves coincide *constructive interference* occurs and, consequently, the magnitude of the final wave increases with respect to the original. On the contrary, when the waves are not in phase, *destructive interference* prevails and hence the amplitude of the resulting wave decreases significantly.

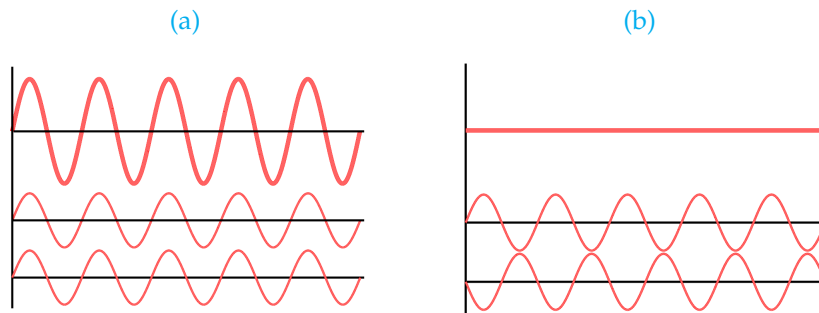


Figure 5.3: Interference effect. (a) constructive interference and (b) destructive interference. Obtained from [47].

### 5.1.3 Modeling of multilayer structures

When light is incident on a multilayer structure, various optical paths can be identified due to internal reflections in each of the interfaces, as depicted in Figure 5.4. If all these interfaces are optically flat, the internal reflection fluxes  $r_i$  and layer transmittances  $\tau_i$  can be calculated by means of the aforementioned Fresnel and Lambert-Beer correlations (Equations 5.3 and 5.5). Once these are known, different strategies can be used in order to obtain the overall reflection ( $R$ ), transmission ( $T$ ) and layer absorption ( $A_i$ ).

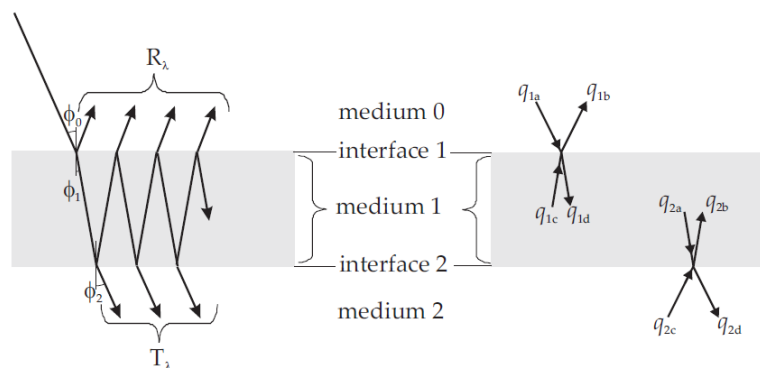


Figure 5.4: Paths of light with it reaches a multilayer structure. Obtained from [19].

For instance, an interesting approach is the *net-radiation method*, which is the core of the GenPro algorithm [19, 36]. This approach consists on grouping all the possible rays around a given interface into four net-radiation fluxes; so that each of them represents the total light intensity due to all possible photon paths for a given direction. This is also illustrated in the previous figure, in which the subscript  $i$  is the interface number whereas the upper subscript ( $a, b, c$  or  $d$ ) indicates whether light is approaching/leaving the interface from its top/bottom.

This method can also be refined in order to consider the presence of thin films and textured interfaces. For further information regarding this approach, please refer the work done by Santbergen, R. [19, 36] and H. Angus MacLeod [46].

## 5.2 Optical filters

Optical filters are devices able to selectively transmit light of different wavelengths. Depending on their working principle, two main types of filters can be distinguished: *absorptive* and *dichroic* [48]. As their name implies, absorptive filters are able to transmit light of certain wavelengths by absorbing the remaining beam component. These filters are frequently made from pigmented gelatin or dyed glass, which confer them the aforementioned features. The ability of the filter to attenuate light is directly affected by both its thickness and the amount of dye present on it.

The main drawback of absorptive filters is that they are not sufficiently precise to be used in certain applications. In addition, their long-temperature resistance is rather poor and they are susceptible to break after prolonged use. Nevertheless, they are affordable devices which have proven to be stable when used in a wide variety of environments.

On the other hand, dichroic filters are substantially more precise devices which are based on the interference principle [49]. This means that as light strikes the filter's top surface, it is immediately splitted into two beams of different wavelengths. This mechanism allows the desired component of light to be transmitted while the remaining fraction is reflected to the surrounding environment. Furthermore, since energy is not absorbed during this process, dichroic filters can be used under light sources up to 280 °C.

The operating principle of both absorptive and dichroic filters is compared in Figure 5.5. As can be observed, for the purpose of transmitting green light (wavelength of around 510 nm), the performance of absorptive filters (Figure 5.5a) is markedly lower since other light components are also transmitted in a lesser extent. On the contrary, it can be seen in Figure 5.6d that dichroic filters are able to almost completely reflect all unwanted beam components and transmit only the target wavelength.

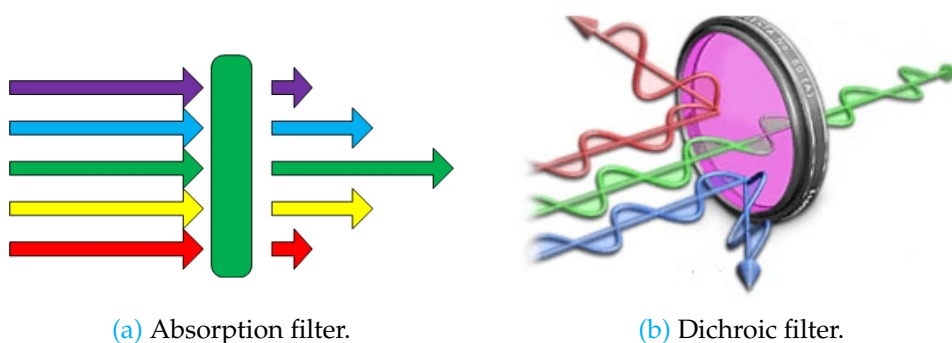


Figure 5.5: Operating principle of two different optical filters which favor the transmission of the green component of light. Adapted from [48].

The superior performance of dichroic filters has triggered their production in the past years. In fact, there are different types available in the market, such as longpass, shortpass, bandpass, and bandblocking filters [50]. Among them, longpass and shortpass filters are able to efficiently block the transmission of bands of short and long wavelengths respectively. In a limit situation, these filters can also behave as cold and hot

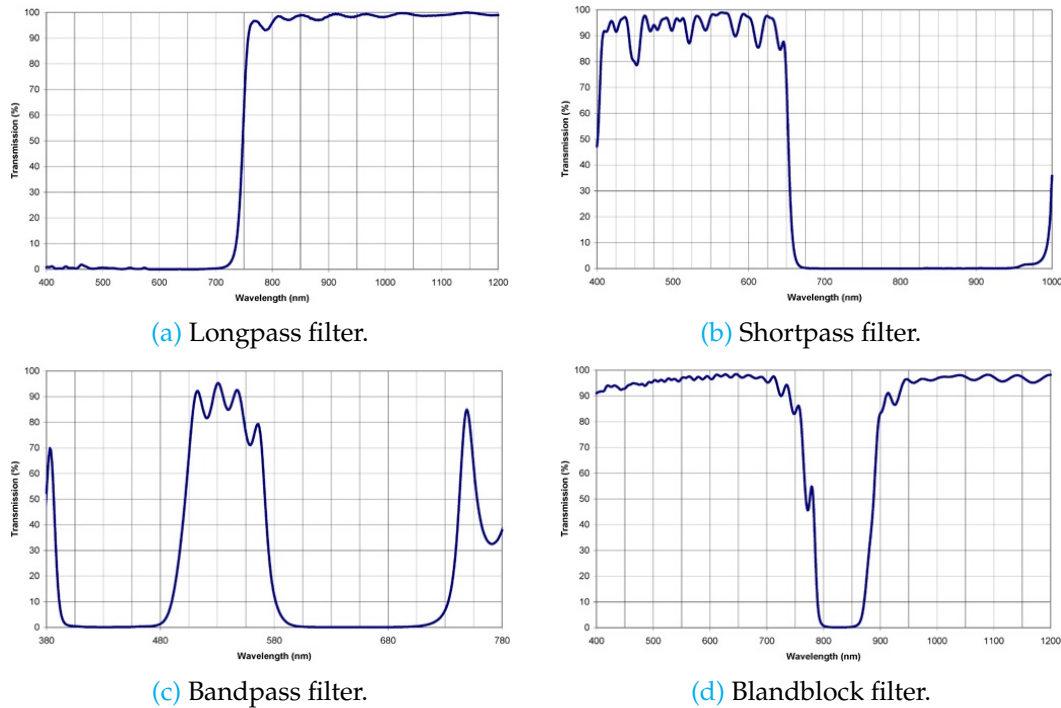


Figure 5.6: Transmission curves for different types of dichroic filters. Obtained from [51].

mirrors, which means that they can either transmit or reflect the near-infrared and infrared (IR) bands [48].

Similarly, bandpass and bandblocking filters offer transmission and reflection throughout a fixed wavelength range. Hence, this type of filter can be used for any given wavelength from near ultraviolet to near infrared. In order to offer a clear view of how each of these filters operate, the transmission curves of some of them have been compiled in Figure 5.6.

For the purpose of this work, dichroic filters are preferable. In particular, provided that the target filter is expected to reflect in an optimum range of wavelengths, the design is made as for a bandpass filter. This guarantees that only infrared components that cause a significant variation in the module temperature are blocked.

### 5.3 Distributed Bragg Reflectors

One of the most straightforward approaches toward the design of an optical filter is based on the use of *distributed Bragg reflectors* (DBR). This type of structure is based on alternating pairs of high and low refractive index materials (frequently denoted by  $n_H$  and  $n_L$ ), each of them with a different thickness.

Optically speaking, a DBR behaves as a one-dimensional photonic crystal (1-D PC). This means that it blocks the absorption and/or transmission of photons in a specific wavelength range, also known as photonic band gap (PBG). The advantage of these structures is that they can be designed in a way that the effective area of reflection is located in the region of interest. In order to achieve this, the starting point of a DBR design is the

selection of a central wavelength of reflection or *Bragg wavelength* ( $\lambda_B$ ). This is followed by the selection of materials and sizing of the structure, as explained down below.

Regarding the selection of materials, it must be first verified that none of them absorb light in the wavelength range of interest. Also, in order to obtain the same reflectance regardless the angle of reflection and polarization, the *omnidirectionality principle* should be fulfilled. This can be reduced to the following condition:

$$n_0' = \frac{n_H n_L}{\sqrt{n_H^2 + n_L^2}} > n_0 \quad (5.7)$$

Following this, the thicknesses of the individual layers can be derived from Equation 5.8 [52]. As can be seen, the optical thickness of each layer (defined as the product of  $d$  and  $n$ ) is a quarter of the Bragg wavelength. This is hence known as *quarter wavelength optical thickness* (QWOT).

$$\lambda_B = 4 d_L n_L(\lambda_B) = 4 d_H n_H(\lambda_B) \quad (5.8)$$

When this condition is satisfied, the reflected waves along the multilayer structure interfere constructively with each other. Consequently, the overall reflection in the wavelength of interest is maximized and the transmission minimized [53].

On the other hand, it is convenient that the difference in the refractive index of both materials around  $\lambda_B$  is as high as possible. This can be derived from Equation 5.9, which defines the reflectance at the Bragg wavelength. Please note that in this formula  $n_0$  and  $n_s$  are the refractive indexes of the incident medium and substrate. Also,  $M$  is referred to the number of bilayers.

$$R(\lambda_B) = \left( \frac{n_0 n_L^{2M} - n_s n_H^{2M}}{n_0 n_L^{2M} + n_s n_H^{2M}} \right)^2 \quad (5.9)$$

In fact, if  $n_0$ ,  $n_s$  and  $\lambda_B$  are fixed and different combinations for the remaining parameters are tried, a result similar to the graph plotted in Figure 5.7 can be obtained. As can be observed, an increase in the difference between  $n_H$  and  $n_L$  has two positive effects. First of all, it leads to higher reflectance values for the same number of bilayers. Furthermore, it requires less layers for achieving a certain reflection, which means that the cost of manufacturing is significantly lower.

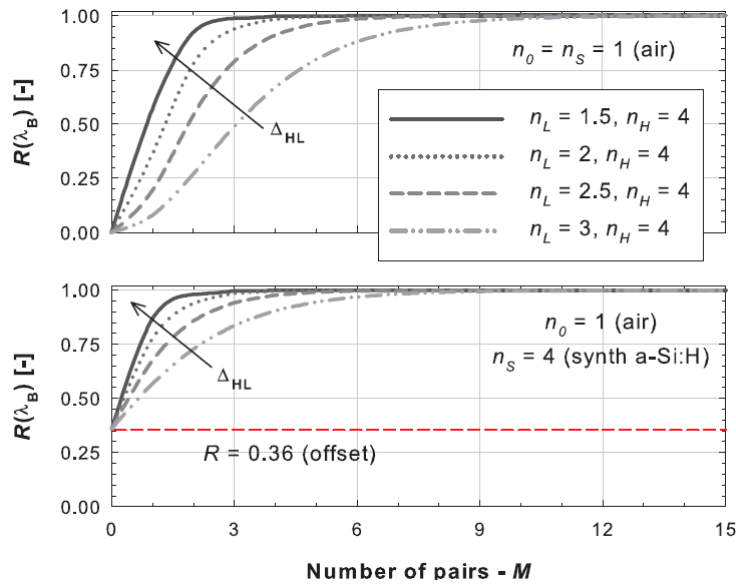


**Figure 5.7:** Reflectance at  $\lambda_B$  as a function of DBR pairs. The set of curves plotted show the effect of different index mismatches for a system based on air/DBR/a-Si:H. Obtained from [52].

In any case, rather than minimizing the number of layers as much as possible, a balance should be found between layers and performance. As  $M$  increases the curve of reflection around the design wavelength is more defined, as depicted in Figure 5.8.

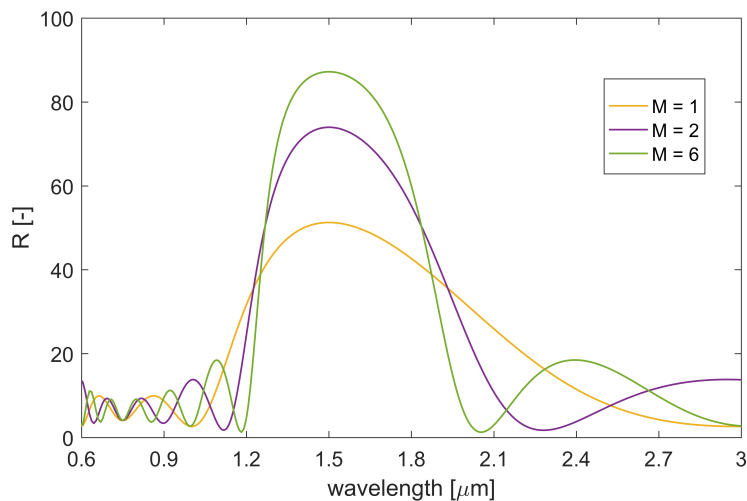


**Figure 5.8:** Reflectance of a DBR for different number of pairs.

## Modulated photonic crystal

However, if the target reflection range is too wide, a single photonic crystal might not be sufficient; even with the highest refractive index difference and number of layers. In this situation, an interesting approach is to use make use of *modulated photonic crystals* [52, 54]. This structure is the result of combining different PC aimed at different design wavelengths, as illustrated in Figure 5.9. Also, this is an alternative solution for obtaining a good reflection profile using materials that do not have a large ratio of refractive indexes.

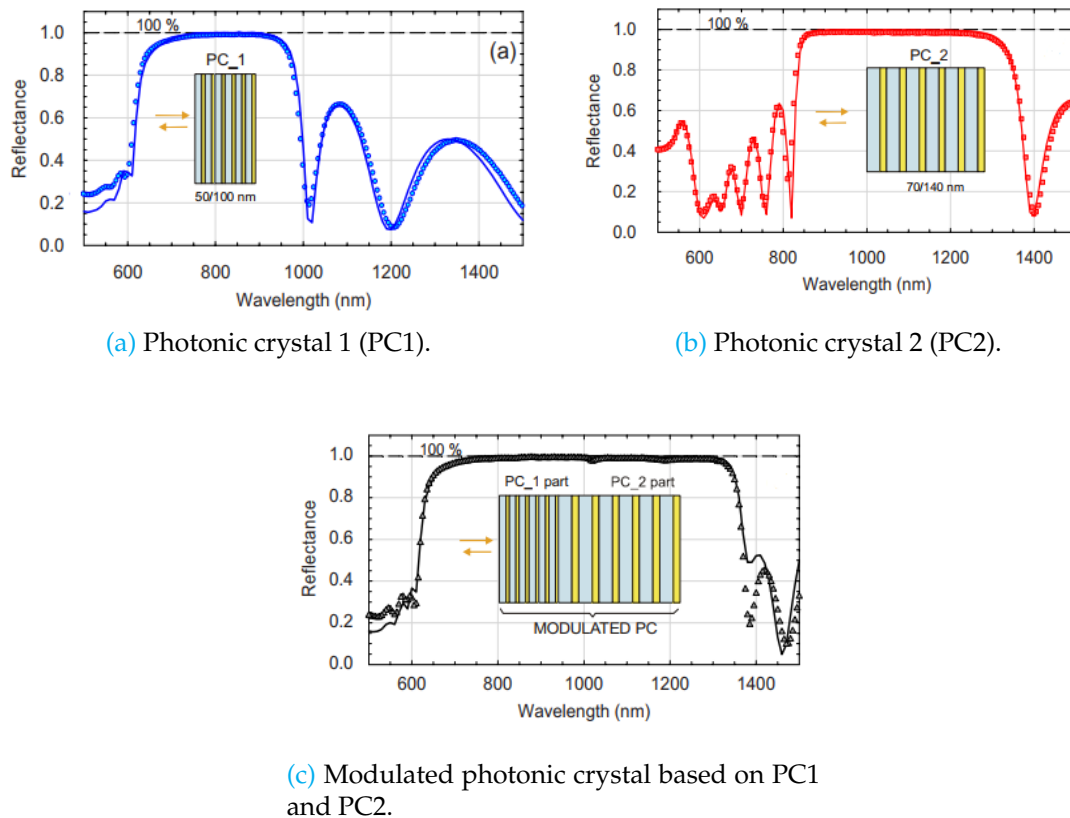


Figure 5.9: Reflectance profile of different photonic crystal structures. Obtained from [54]

## 5.4 Needle technique

This optimization technique was firstly described at the beginning of the eighties, but only a decade after it started to be widely used. Since the mathematical formulation of this method is rather complex, the aim of this section is just to provide the reader with a general understanding of the operating principle and physics involved. For further information, please consult references [55, 56].

Basically, this optimization method is based on the addition of thin films into optimal positions within an initial multilayer structure [56]. If these films are inserted in the right places, the new interference effects associated with them will lead to an improvement on the spectral response of the stack.

From this basis, it can be seen that the core of the needle technique is finding the adequate positions for inserting new layers. This decision is made based on the impact of a given change over the so-called *merit function* ( $F$ ). This parameter gives a measure of the difference between the actual reflection response and the target one, as stated in Equation 5.10 [55]. In this formula,  $w_m$  is a weight factor and  $R$  and  $\tilde{R}$  denote the actual and desired reflectance over a given set of wavenumbers,  $k_m$  ( $m = 1, \dots, M$ ). Also,  $\bar{X}$  is referred to the any set of control parameters, for instance refractive indexes or layer thicknesses.

$$F(\bar{X}) = \sum_{k_m} w_m [R(k_m) - \tilde{R}(k_m)]^2 \quad (5.10)$$

Therefore, the needle technique is based on minimizing the merit function by adding intermediate layers in the most adequate positions. After a layer is inserted, its thickness is progressively changed until the merit function cannot be further minimized. Once this have been done, more layers are added and adjusted until the problem converges. That is, until the lowest value of the merit function has been reached. This iterative process is simplified in Figure 5.10

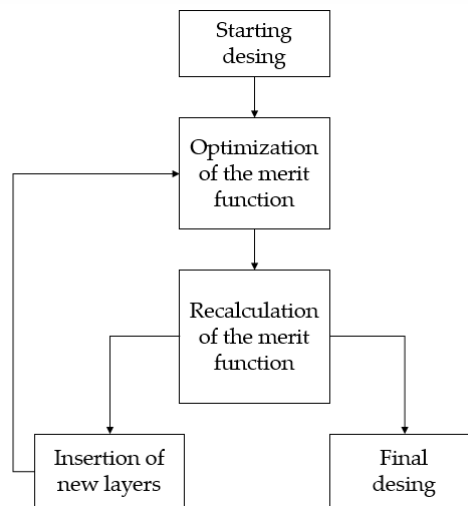


Figure 5.10: Iteration scheme of the needle technique method.

Nowadays, there are multiple softwares available that operate according to the needle approach. A remarkable example is Open Filter; an open source software developed under the GNU General Public License [57]. This tool has been proven to be a good option for the optimization of thin film multilayer structures [58].

## 5.5 Fence Post Method

The Fence Post (FP) method can be defined as an optimization strategy for multilayer structures based on QWOT [59, 60]. The name of this technique is based on the characteristic plot obtained when representing the refractive index versus the film thickness.

As can be seen in Figure 7.15, the plot looks like a thin fence posts of high index material separated between each other and standing above a ground of low index material.

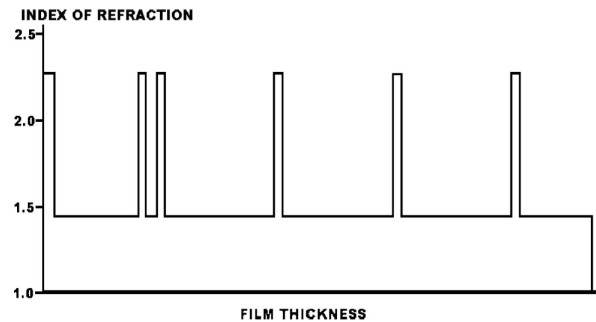


Figure 5.11: Index of refraction as a function of thickness for a typical Fence Post design. Obtained from [59].

This technique has been initially developed for the manufacturing of anti-reflective coatings. In this case, the FP approach has led to a good broad band of reflection and improved the scratch resistance of the final structure. Since these early applications, the use of this tool has been expanded to, for instance, edge filters, blocking filters, narrow bandpass filters, etc.

As for the needle technique, the starting point of the Fence Post method is a multi-layer structure based on QWOT. For these cases, it can be proven that the width of the blocking band decreases as the ratio of the overall thickness to the thinnest layer becomes greater than 2:1 [59]. This can be a problem during the design of filters aimed at high wavelengths, since the lower performance should be compensated by adding more layers to the structure.

In order to tackle this, the Fence Post method is based on fixing the thickness of the high-index material (which is the lowest one) and vary all the low-index thickness independently [59]. Based on the previous diagram, this can be interpreted as keeping all the fence posts at the same size and modifying the distance between them.

This design approach can also be implemented in the software Open Filters. In order to do this, a structure based on QWOT must be firstly defined. Then, it is possible to select the layers whose thickness needs to be optimized: which in this case are the low-index material layers.



## Chapter 6

# Experimental setup

The objective of this section is to present the most relevant tools used for the deposition and optical characterization of films. First, further insight is given on the thermal evaporator used. Afterwards, spectroscopic measurements are introduced

### 6.1 Thermal evaporator: PROVAC

Thermal evaporation has been used for depositing the test filters described in the previous section. In particular, the equipment used for this purpose is the PROVAC PRO500S. This system enables the evaporation of materials via either electronic beam (e-beam) evaporation or thermal evaporation. In the case of titanium dioxide and magnesium fluoride, the first of these options was used. This is due to the fact that the deposition process was already optimized and that, in the case of  $\text{TiO}_2$ , better optical properties were obtained.

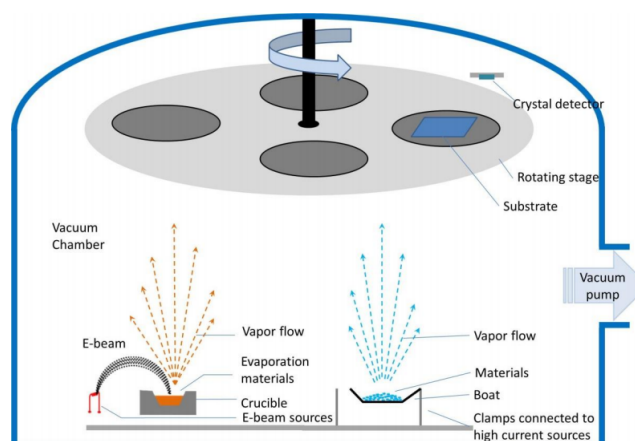


Figure 6.1: Schematic representation of the deposition chamber in PROVAC. Extracted from [61].

An schematic representation of PROVAC is presented in Figure 6.1. As can be observed, the sources of electron beam and thermal evaporation are located at the left and right sides of the equipment respectively. During e-beam evaporation, the material is placed in one of the four available ceramic crucibles. Afterwards, a current of electrons is directed towards the material, causing it to heat up first and subsequently evaporate. Differently, materials that are deposited via thermal evaporation are generally placed in a boat structure (most of the times made of tungsten) which is progressively heated until the material starts to evaporate. This method requires substantially less energy and hence is normally used for depositing materials with a low melting point.

As it evaporates, the material rises towards the rotating disk placed at the top of the equipment, in which the substrates are placed. As the atoms interact with the cold substrate, they start to condense thus leading to the formation of a thin film. This process is carried out in vacuum to prevent interaction with any other particles. To this regard, values in the order of  $10^{-5}$  mbar are normally used, being  $2 \cdot 10^{-5}$  sufficient in most of the cases.

## 6.2 Spectroscopic ellipsometry

Spectroscopic ellipsometry (often shorted as SE) measurements were carried out in order to determine the optical properties of the films deposited, namely refractive index and extinction coefficient. For this purpose, the following equipment has been used: A M-2000 Ellipsometer, by J. A. Woollam Co.

The operating principle behind this technique lies on determining the change of direction in a beam of light upon reflection at a given surface [61]. In particular, the incident ray is decomposed into its s- (perpendicular) and p- (parallel) components. By measuring the relative difference between these two components (based on amplitude, thickness of the sample, etc.) it is possible to obtain the internal reflections of light by means of the Fresnel equations. This can be subsequently expressed in form of refractive index and extinction coefficient.

Finally, these values are computed and approximated to the best fit.

## 6.3 Determination of reflection, absorption and transmission: Lambda

The last equipment used is the Perkin Elmer Lambda 950 spectrophotometer. These measurements were carried out in order to characterize samples that were too thick for being tested via SE. An example of this is the 3 mm KG-3 glass used as a substrate.

The main components in this equipment are a tungsten-halogen light source (able to emit at wavelengths between 175 and 3500 nm) and an integrated sphere (Figure 6.2). This last tool is used to analyze the different paths followed by a beam of light project onto a certain surface. In particular, the inner side of the sphere is coated with a highly reflective material which allow the identification of all the rays transmitted through a

given material. Ultimately, the fraction absorbed can be obtained by comparing the projected and transmitted rays.

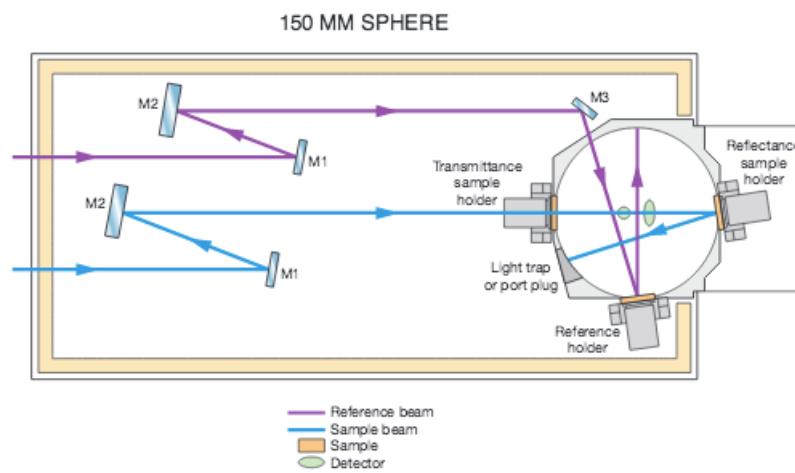


Figure 6.2: Schematic representation of an spectrophotometer. Extracted from [62].



## Chapter 7

# Design and fabrication of the optical filter

### 7.1 Optical filter design

Given the potential of infrared optical filters as a temperature-control element, the purpose of this section is to design and build a multilayer structure able to block the undesired components of light, i.e. in between 1100 and 2500 nm. First, the most appropriate materials are selected and their optical properties are discussed. Afterwards, different designs are made along with the experimental depositions.

#### 7.1.1 Selection of materials

The first choice of materials for the design and construction the infrared optical filter are magnesium fluoride ( $\text{MgF}_2$ ) and titanium dioxide ( $\text{TiO}_2$ ). These materials are well-known due to their particularly low and high refractive index. For the magnesium fluoride, this is approximately 1.30 while for titanium dioxide in can vary between 2.25 and 2.65 depending on the deposition conditions [46].

The substantial difference in their refractive indexes suggests that this combination of materials is an interesting option for the design of an optical filter. As discussed in Chapter 4, this is due to the fact that less layers would be needed to achieve the desired performance. This feature is even more interesting for the case of infrared filters, since the layers are usually thicker at increasing wavelengths. Hence, a balance can be achieved between manufacturing complexity (directly proportional to the material needed) and performance.

#### Influence of annealing

Following the selection of materials, individual layers of magnesium fluoride and titanium dioxide were deposited in order to measure their optical properties; namely refractive index and extinction coefficient. Then, the influence of annealing in all samples was assessed and, finally, the most convenient deposition methods were identified.

To begin with, the magnesium fluoride film was deposited via electronic beam evaporation. This method has proven to be the most appropriate for this material since the resulting layer is less susceptible to optical loss [63]. On the other hand, for the titanium dioxide both thermal and electron beam evaporation were investigated. Following this, all films were annealed at 400 °C in air for a period of 30 minutes, as suggested in reference [64].

The resulting refractive indexes of magnesium fluoride and titanium dioxide are presented in Figures 7.1 and 7.2. To this regard, it is important to point out that the spectral ellipsometry measurements only covered the range of wavelengths between 190 and 1690 nm. For higher values, it has been assumed that neither the refractive index nor the extinction coefficient vary significantly. This is also suggested by the shape of the obtained curves.

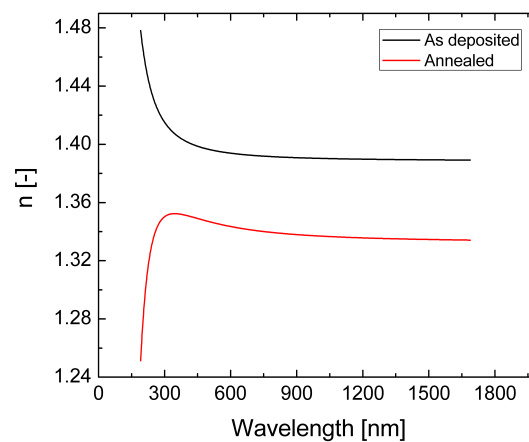


Figure 7.1: Refractive index of magnesium fluoride deposited via thermal evaporation. Values for the film as deposited and annealed.

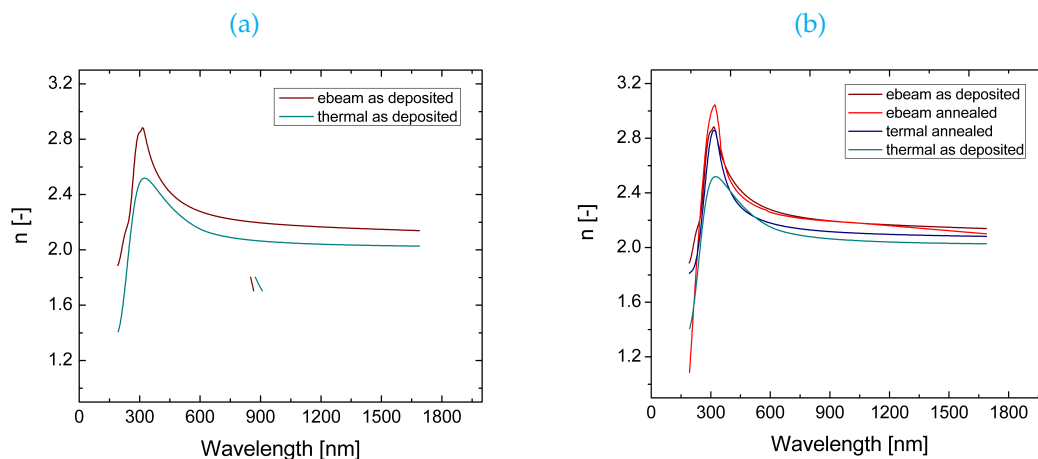


Figure 7.2: Refractive index of titanium dioxide deposited via thermal and electron beam evaporation. (a) as deposited and (b) after annealing.

In the case of magnesium fluoride, it has been found that the refractive index decreases slightly as a consequence of annealing. For high wavelengths, a decline from 1.39 to

1.34 is observed. Regarding the extinction coefficient it could be observed that, as expected, its value is equal to zero for the entire wavelength range. This implies that none undesired light absorption occurs and hence the filter design is not hampered.

A similar result has been obtained for the case of titanium dioxide. Indeed, it can be observed from Figure 7.2a that for the area of interest the refractive index increases from 2.0 to near 2.2. This behavior is in accordance with the results reported in the literature. In fact, it has been shown that the refractive index of titanium dioxide increases proportionally with annealing, until it reaches a maximum at around 3.0-3.5 [65, 66].

On the other hand, it can be seen from Figure 7.3 that the extinction coefficient is practically the same for thermal evaporation and electron beam evaporation. In both cases, this value is slightly higher than zero for wavelengths below 500 nm. This is particularly true for as deposited films, since a significant reduction has been measured for the annealed samples.

Unlike the refractive index, the impact of annealing over the extinction coefficient does not follow a clearly defined trend. This can be explained based on the existence of two different phases at high temperatures: *anatase* and *rutile*, as illustrated in Figure 7.4.

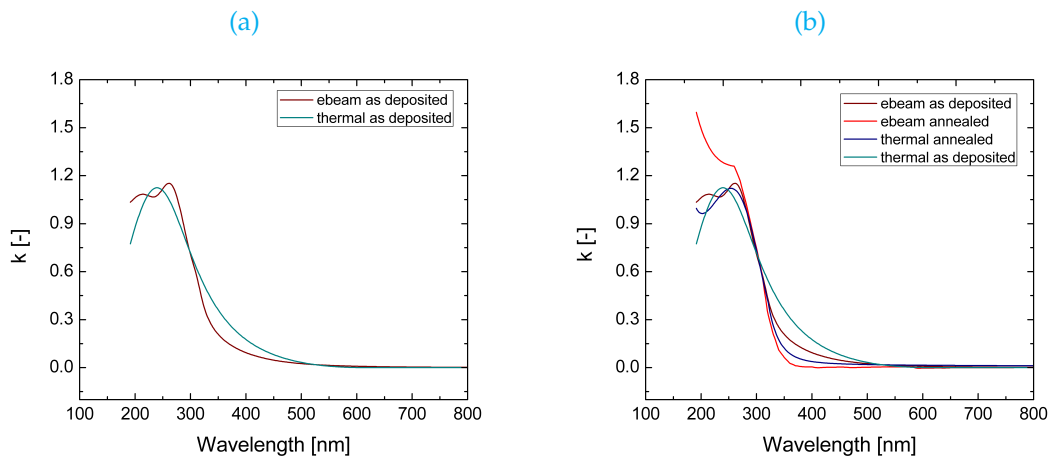


Figure 7.3: Extinction coefficient of titanium dioxide deposited via thermal and electron beam evaporation. (a) as deposited and (b) after annealing.

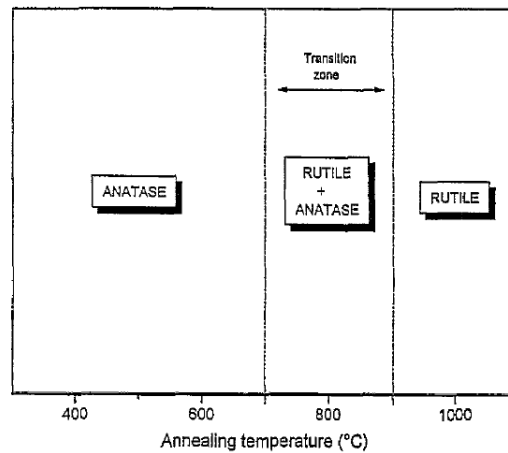


Figure 7.4: Titanium dioxide phase transition diagram a function of annealing temperature. Adapted from [65].

In particular, it can be observed that the anatase phase persists for annealing temperatures comprised between 300 and 700 °C. As the temperature increases, an equilibrium area between the two phases is firstly reached, until all the titanium dioxide is converted into its rutile form at around 900 °C onwards [65].

When titanium dioxide is deposited at ambient temperature, the resulting film is generally in its amorphous phase. At increasing annealing temperatures, the material crystallizes first in the form of anatase and then in the form of rutile. Depending on which phase is dominant, the effect of annealing over the extinction coefficient is different. In fact, it has been reported that during the transition from the amorphous to the anatase phase, an increase in the temperature causes a decrease in the extinction coefficient. On the contrary, in the transition region, higher temperatures yield higher extinction coefficients [65].

This argument can explain the decrease in the extinction coefficient after the annealing treatment (Figure 7.3b). Under these circumstances, the deposited film would have crystallized in the anatase form. This result is convenient for the design of the optical filter, since the smallest absorption at lower wavelengths can compromise significantly the transmission of light. Taken this into account, the preferred deposition method for titanium dioxide is electron beam evaporation. This is because either with annealing or not, the extinction coefficient in the wavelength range between 300 and 500 nm is lower than the respective of thermal evaporation.

### 7.1.2 Preliminary designs

This section gives an overview of the preliminary filter designs. This comprises the first approaches based on elemental optical theory and subsequent optimizations. Please note that, in all cases, standard soda lime glass was used as a substrate.

### Modulated Bragg reflector

Considering that the ideal wavelength range of reflection is rather wide (from 1100 to 2500 nm), the first approach followed was based on the use of a modulated distributed Bragg reflector. In particular, a multilayer structure based on three DBR was developed. In order to cover most of the desired wavelength range, each of these intermediate filters were aimed at the following design wavelengths: 1300, 1650 and 2100 nm.

Following the design rules presented in Section 5.3, a filter comprised of eighteen layers was firstly designed. This is a combination of six layers per individual Bragg reflector. The characteristic thicknesses of each reflector are presented in Table 7.1. As in standard structures, this stack can be represented by the following scheme: air | HLHLHL...HL | glass. This indicates the sequence in which the high and low refractive index materials are structured.

**Table 7.1:** Specifications of an optical filter based on three modulated Bragg reflectors. The high and low refractive index materials are titanium dioxide and magnesium fluoride.

	DBR 1	DBR 2	DBR 3
$\lambda_B$ [nm]	1300	1650	2100
$d_{TiO_2}$ [nm]	142	182	233
$d_{MgF_2}$ [nm]	237	302	393

As can be observed in Figure 7.5a, this structure is able to reflect nearly 80% of the incident light in the wavelength range between 1100 and 2000 nm. However, for higher wavelengths the performance is less satisfactory. In order to minimize this, more layers were added to the intermediate structures. This only lead to a small increase of reflectance at wavelengths between 1100 and 2000 nm, which was characterized by a high performance.

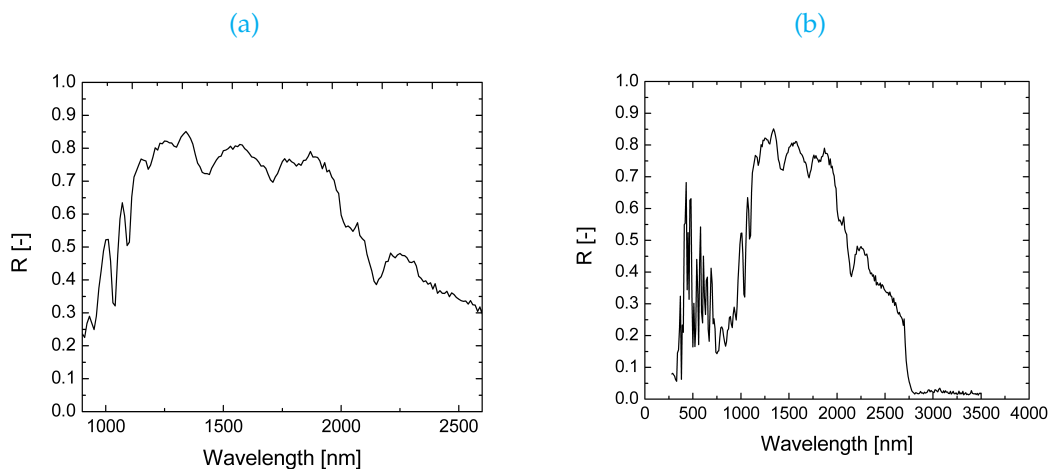


**Figure 7.5:** Reflectance profile of an infrared filter based on three modulated Bragg reflectors. (a) detail (1100-2500 nm) and (b) overview (280-3000 nm).

In addition to this, this filter was found to be inappropriate on account of reflection of light around 500 nm, as depicted in Figure 7.5b. This would imply that a fraction of usable energy would not even reach the solar cell, hence leading to a significant decrease on the photogenerated current and hence overall performance. An estimation of these losses is presented in Figure 7.6. As can be seen, the cell efficiency in this scenario would drop from around 20 to 15%.

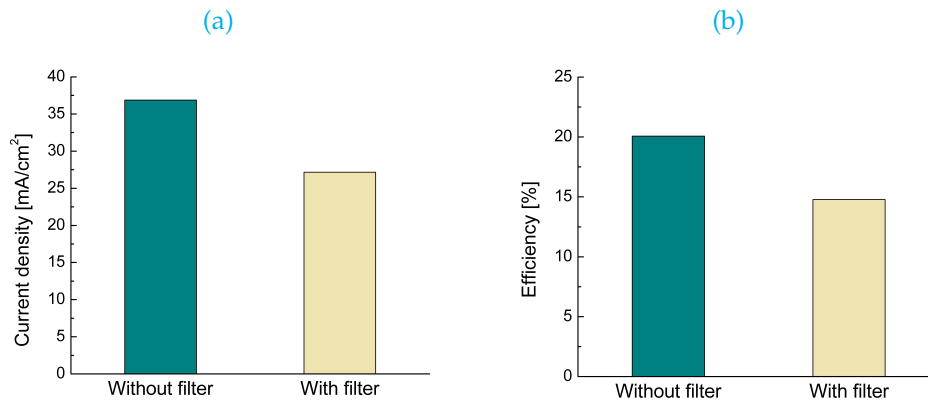


Figure 7.6: Influence of a modulated optical filter over the performance of a solar cell. (a) photogenerated current and (b) cell efficiency.

This phenomenon has been previously reported in literature [67, 68]. In these cases, the possibility of changing the standard design pattern (HLHLHL...HL) is suggested. Such approach allows a significant reduction of the reflection ripple presented between the peak of reflection and the target reflection. However, for actually canceling the peak more refined iterative methods need to be used.

### Optimization: needle technique

In order to cancel the peaks of reflection in the visible, the needle technique (Section 5.4) is used for optimizing the previous design. As previously discussed, this implies the addition of intermediate layers within the already existing structure. Therefore, it can already be predicted that the higher the number of layers, the better the performance of the filter would be compared to the target structure.

Indeed, for a nearly perfect filter it was found that the total number of layers should be higher than 150. For instance, the structure presented in Figure 7.7 is comprised of 156 layers. As can be observed, the reflectance is around 90% for the area of interest. Besides, the undesired peaks of reflection in the visible were effectively canceled during the optimization.

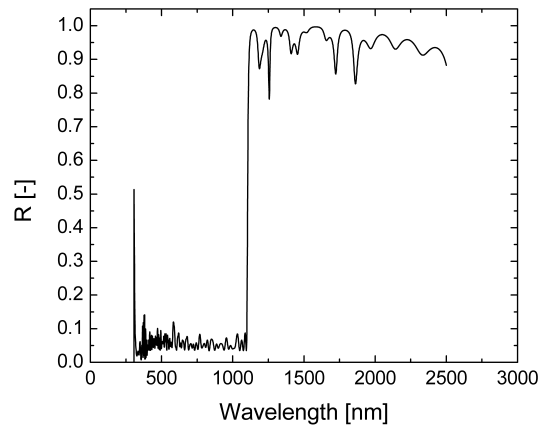


Figure 7.7: Reflectance profile of a 156 layer optical filter optimized via needle technique.

In spite of the advantages that this filter offers, its elevated number of layers make it rather difficult to manufacture. Based on this, an alternative approach is to narrow down the area of reflection to 1100-2000 nm. This option allows a reduction in the number of layers without sacrificing the module temperature; which would be around 1 °C higher according to Figure 4.7b.

For this particular case, the optimization study revealed that around 90 layers would be needed. An example of such structure is depicted in Figure 7.8. As in the previous case, it can be observed that a good reflectance is achieved for the area of interest while keeping the peaks of reflection in the visible at a minimum.

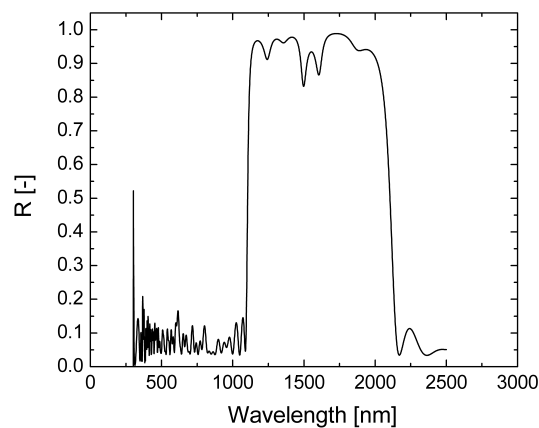


Figure 7.8: Reflectance profile of a 92 layer optical filter optimized via needle technique.

### Design of a test filter

In order to evaluate the deposition of a filter based on magnesium fluoride and titanium dioxide, a set of test filters was designed. In these structures, the number of layers is kept to a minimum in order to facilitate the deposition. This is because only a small amount of material could be placed on the thermal evaporator crucible at a time. Hence,

for a more complex structure the overall process would need to be subdivided into more than ten intermediate depositions, which would be extremely time consuming.

To begin with, a minimum of 50 layers was set. Based on this limitation, the best approximation to the target filter was found to be a 44 layer structure. As depicted in Figure 7.9, the performance of this filter in the area of interest is lower than as for the previous design, with an average value between 0.7 and 0.8. Apart from this, the peaks of reflection at lower wavelengths were mostly suppressed, even though the result is not as optimum as for the previous designs.

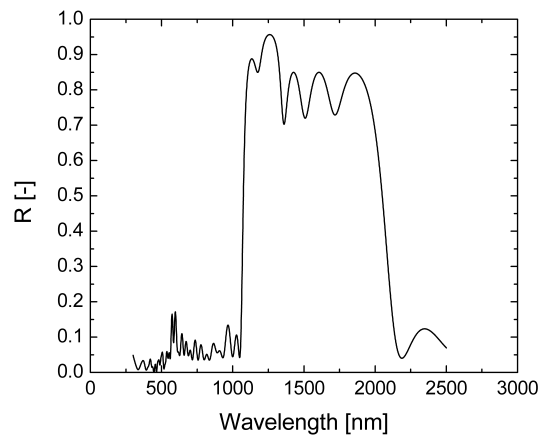


Figure 7.9: Reflectance profile of a 44 layer optical filter optimized via needle technique.

When the number of layers was decreased further than this, it was not possible to minimize the undesired peaks of reflection. Based on this result, the focus was shifted towards finding a structure able to effectively block light in the area of interest, regardless of the peaks at lower wavelengths. This decision was made to facilitate some preliminary depositions and to evaluate the feasibility of thermal evaporation for the fabrication of the filter. The conclusions drawn from these experiments could then be applied to a more precise design.

Considering this, the main option for testing was the initial filter based on QWOT. Alternatively, a slightly more optimized version of this structure was obtained via needle technique. This was done in order to increase the reflection in the desired range while keeping the addition of layers at a minimum. The resulting filter is depicted in Figure 7.10. As can be seen, around a 90% of light in the range of 1100 to 2000 nm is reflected.

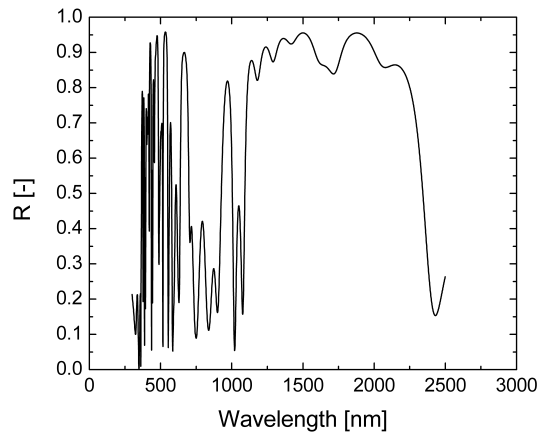


Figure 7.10: Reflectance profile of a 20 layer optical filter optimized via needle technique.

### 7.1.3 Construction of the test filter

Among all the test filters designed, the alternative based on 20 layers (Figure 7.10) was chosen for the first deposition. This decision was made based on the simplicity of the structure combined to the fact that a better performance is achieved in the area of interest.

For this purpose, the regular glass substrate was substituted by an infrared-absorbing glass. This decision was made in order to measure a significant change in temperature in case the multilayer structure was effectively deposited. In fact, preliminary thermal simulations revealed that the absorption of infrared light in the standard glass (700  $\mu\text{m}$ ) used in the laboratory is negligible. This would only be noticeable in case the glass thickness was in the order of micrometers, which was not available at the time.

Therefore, the filter design was firstly re-adapted to this substrate. Also, some minor corrections in the individual layer thicknesses were done in order to compensate possible deviations in the quantity of material released during evaporation. In fact, the film characterizations done via spectroscopic ellipsometry revealed that titanium dioxide films were around 20 nm lower than expected while magnesium fluoride was generally 5 to 7 nm higher.

In order to guarantee that the material in the crucible was never depleted, the deposition was subdivided in three intermediate steps. After the first of them (which implied the deposition of seven layers), it was found that the layers deposited until the moment were delaminating, as can be seen in Figure 7.11. This result reveals the existence of large mechanical stresses across the multilayer structure.



**Figure 7.11:** Stress in a flat-glass substrate sample after the deposition of seven layers. Some particle remains can be seen on the lateral side.

In order to tackle this, the first approach considered was to deposit a 100 nm film of indium tin oxide (ITO) on top of the substrate and etch it in an acid bath afterwards. For this purpose, a solution based on hydrofluoric acid (5%) and hydrogen peroxide was used. The objective of this experiment was to induce a textured surface on the substrate. This would provide some additional structural support to the stack and hence lead to a slight reduction in the mechanical stress.

However, no relevant changes were observed after around 20 minutes of etching. Based on this, the next approach was based on achieving a similar textured surface on a ZnO:Al (AZO) film. For this purpose, a 1  $\mu\text{m}$  thick layer was firstly deposited via plasma enhanced chemical vapor deposition (PECVD) and etched afterwards for 25 seconds. The final thickness after etching is expected to be around 700 nm [69]. This is likely to lead to some unwanted absorption, but a further reduction in the original thickness is not feasible since it would difficult the controllability of the etching process.

In addition to this, a thin layer of chromium was added in one of the samples in order to motivate the adhesion between the individual layers. Such layer was deposited in between the glass and the AZO film.

In order to evaluate whether or not a different substrate would be favorable, two additional crystalline silicon wafers were used. One of them completely polished and the other with a smooth texture.

Just as in the previous case, the constituent films were found to be delaminating at some point during the deposition. For the crystalline silicon samples, this happened rather soon: just after the first four layers were deposited. It should be noted that, nonetheless, the mechanical stresses were less visible in the textured wafer. However, there is no image evidence of this since the wafers were immediately removed due to the toxicity of magnesium fluoride. This was also done to avoid possible errors due to the release of material from these samples. After doing this, the deposition was continued for the remaining glass samples.

Similar than in the previous case, for these samples it was observed that some delamination was induced after the deposition of eight layers. This can be observed in Figure 7.12. Comparing both samples, it can be seen that the effect of chromium was not as positive as expected. In fact, the sample without chromium shows a less pronounced delamination.

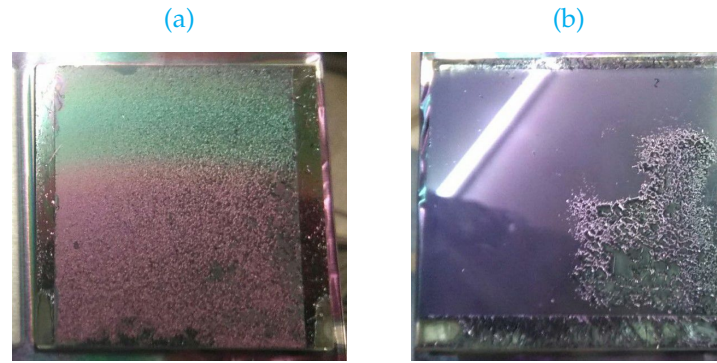


Figure 7.12: Stress in the samples after the deposition of eight layers. (a) textured glass with chromium and (b) textured glass without chromium.

This result is slightly better than the one obtained after the first deposition. This suggests that, in fact, inducing a texture interface can reduce the mechanical stresses across the substrate. Nonetheless, this solution is not sufficient towards future depositions; in which filters based on more than 20 multilayers would need to be deposited.

#### 7.1.4 Discussion

The pronounced mechanical stress in multilayer structures based on titanium dioxide and magnesium fluoride has been previously addressed in the literature [64, 70, 71]. The exact reasons behind this phenomenon are not completely known, but most experimental evidence suggests that the deposition methods and substrate temperature may play an important role towards achieving a stable structure.

With regard to the deposition methods, a promising solution is based on *plasma ion-assisted deposition* methods (PIAD), as described in reference [64]. In particular, this study provides experimental evidence about the benefits of switching from electron-beam to PIAD for depositing the  $\text{TiO}_2$  films. When this was done, it was verified that almost no microcracks were presented along the structure. As can be seen in Figure 7.13b, this is a substantial improvement with respect to the as deposited e-beam films (Figure 7.13a).

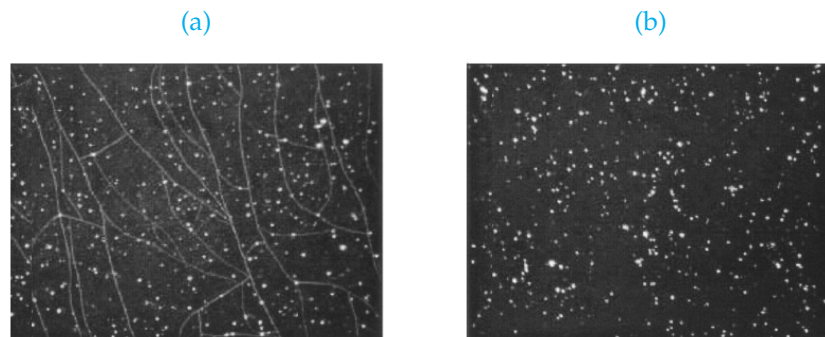


Figure 7.13: Surface figure of a  $\text{TiO}_2/\text{MgF}_2$  stack deposited via: (a) electron-beam evaporation (b) plasma-ion assisted deposition. Obtained from [64]

This is argued to be due to a transition from tensile stress to compressive stress in the titanium dioxide films. Under these circumstances, the tensile stress of electron-beam deposited  $\text{MgF}_2$  would be compensated and hence the multilayer would be more stable.

In addition, it was observed that switching to PIAD also has a positive effect over the resulting film microstructure [64, 70, 71]. More specifically, when both titanium dioxide and magnesium fluoride are deposited via electron-beam evaporation the resulting film is particularly porous; with a packing density between 0.7 and 0.8. On the contrary, if both materials are deposited via PIAD, the packing density has been found to be close to unity [71]. This minimizes moisture absorption in the voids of the structure and hence improves the overall stack stability [64]

A similar approach has been proposed by S. H. Woo *et al.* [70]. The main addition to the previous idea is based on heating the substrate up to  $140^\circ\text{C}$ , resulting in a stress reduction from around 168 MPa to 126 MPa.

Even for individual films of titanium dioxide and magnesium fluoride, it has been proven that the quality of the deposited films is better when the substrate is at a high temperature [46]. For the  $\text{MgF}_2$ , values between  $200$  and  $300^\circ\text{C}$  are recommended while for the  $\text{TiO}_2$  better results on glass are achieved when the temperature is maintained around  $200^\circ\text{C}$ . In addition to this, it is convenient that the temperature during the deposition is kept constant. Otherwise, thermal stresses can arise due to variations in the heat expansion coefficients of both the film (or multilayers) and substrate [72].

In fact, this is likely to occur when films are deposited in PROVAC. This is because the temperature of the substrate and deposited films is constantly changing: from ambient temperature to higher values reached during the evaporation of the materials. Unfortunately, the inside temperature can neither be monitored nor maintained constant.

In addition to the aforementioned factors, it has been found that the  $\text{MgF}_2/\text{TiO}_2$  stacks deposited in PROVAC are not sufficiently uniform. This effect was explored by depositing a simple (4 layers) structure comprised of thin layers (around 50 nm). As can be seen in Figure 7.14, the color degradation indicates a gradient of thickness along the sample.



**Figure 7.14:** Color degradation in a multilayer structure based on magnesium fluoride and titanium dioxide. This effect indicates that the surface is not uniform.

### 7.1.5 Alternative methods

All these cases, nonetheless, are based on narrow band pass filters (comprised of thin layers). Hence, an additional limitation during the deposition of the infrared filter is due to thicker layers. An alternative solution in this case is to redesign the filter according to the Fence Post method. In particular, for a multilayer structure based on  $\text{MgF}_2$  and  $\text{TiO}_2$  it is convenient to optimize the layers of magnesium fluoride films, since these are the thicker.

Following this approach, it is possible to obtain the reflectance profile depicted in Figure 7.15. This is an eighteen layer filter than could, in principle, be used for testing purposes. Nevertheless, since the uniformity of the layers deposited via thermal evaporation is not sufficient, alternatives based on different materials and methods are more promising.

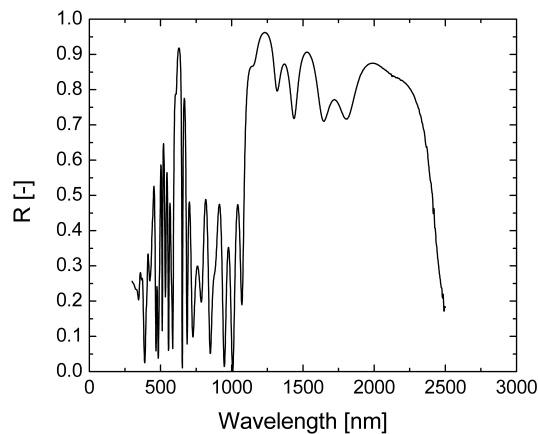
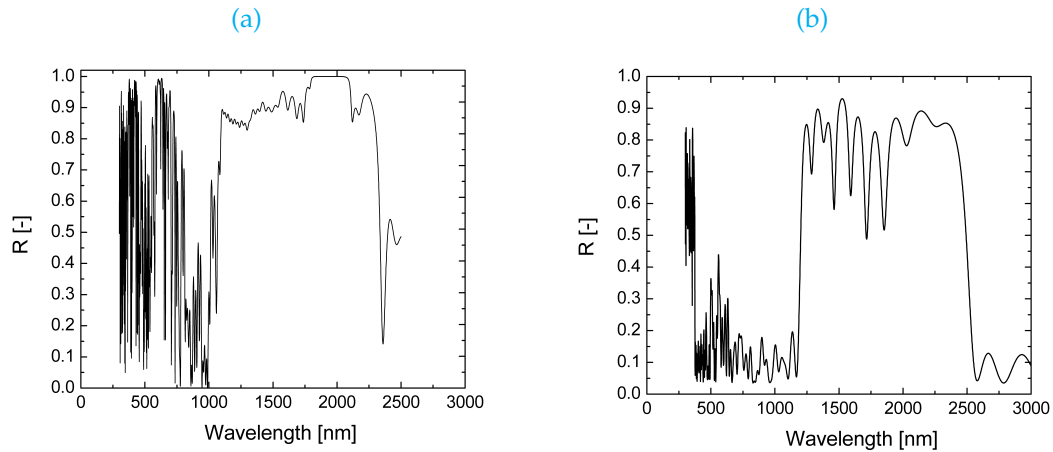


Figure 7.15: Reflectance profile of a 18 layer optical filter optimized via the Fence Post method.

To this regard, an interesting option is based on the use of silicon nitride and silicon oxide layers as high and low refractive index materials respectively. In terms of fabrication, this structure could be deposited via plasma-enhanced chemical vapor deposition (often shortened as PECVD). This approach presents the advantage of a better film uniformity, as assessed in previous studies [10, 45]. In addition to this, it has been proven that by tuning the ratio of ammonia to silane during the deposition, the refractive index of silicon nitride could increase up to 1.98 for the wavelength range of interest [73].

Even in this case, the difference in the refractive index of these materials (nearly 0.5) would be lower than in the case of magnesium fluoride and titanium dioxide, which implies that more layers would be needed for achieving the same reflectance profile. However, both silicon nitride and silicon oxide are currently used in the PV industry and, as mentioned before, their deposition is more likely to be standardized.

Under these premises, the needle technique optimization has been used in order to design both a simple structure aimed at testing and a more complex infrared filter. The results from these simulations are presented in Figure 7.16. As can be seen, these materials also require the use of non-conventional design methods due to pronounced peaks of reflection at lower wavelengths. However, optimization techniques can be successfully used for designing a filter near the target.



**Figure 7.16:** Reflectance profile of an infrared filter based on silicon nitride and silicon oxide. (a) test filter (60 layers) and (b) optimized design (108 layers)

## Chapter 8

# Conclusions and recommendations

In this project, a passive approach to reduce the operating temperature of crystalline silicon modules has been presented. This approach relies on the use of optical filters to partially block the absorption of infrared light. At these wavelengths, the energy content of the absorbed photons is not sufficient to overcome the bandgap of silicon ( $\sim 1.12$  eV, 1100 nm). Therefore, this energy does not contribute to the electrical output of the cell and hence only causes an unnecessary warming of the module.

Instead of blocking most of the infrared component, the aim of this project was to determine the optimum wavelength range of reflection. This represents a compromise between performance and manufacturing simplicity. For this purpose, a thermal model has been firstly developed in COMSOL Multiphysics. This tool enabled a thorough analysis of all the heat transfer mechanisms involved during normal operation of PV modules. In addition, these simulations were supported by a ray tracing evaluation from which the absorption coefficients of all the constituent layers of the module were retrieved.

In order to determine the optimum range of reflection, the impact of light absorption at different wavelengths was analyzed. These simulations revealed that thermalization accounts for the main source of heat within a module. Nevertheless, it was proven that absorption of light beyond the bandgap of silicon causes an additional increase of around 6 to 7°C in the module temperature. In particular, it was observed that from 2500 nm onwards, the energy of the absorbed photons is extremely low and hence does not have a significant impact over the module temperature. Based on this, it was concluded that the ideal wavelength range of reflection is located between 1100 and 2500 nm.

The total reflection of light in this wavelength range can notably affect the performance of a PV module. To this regard, it was found that the contribution of an infrared filter is significantly higher in climates characterized by high irradiance levels and severe meteorological conditions, namely low wind speed and elevated ambient temperature. Under these circumstances, an increase between 2 and 2.5% over the yearly energy production is expected. Such improvement could be particularly interesting in large scale photovoltaic installations.

With regard to the optical filter design, different methods were used along this project; from basic approaches based on QWOT to more complex optimization techniques. In

all cases, binary multilayer structures based on magnesium fluoride and titanium dioxide were modeled. These materials were chosen based on the high difference between their refractive indexes. From the point of view of design, it was proven that a multilayer structure based on 90 to 100 layers could reflect up to 90% of the incident light. For simplicity purposes, a simpler structure based on 44 layers could be used instead. Even though this filter only reflects light between 1100 and 2000 nm, the significant reduction in the number of layers makes it an interesting alternative in terms of construction. However, subsequent depositions revealed significant complications during the fabrication of the structure. This was found to be a combination of the high tensile stress between the thin layers and inadequate deposition methods.

Based on this result, alternative materials and methods should be investigated. As suggested by Macleod's [46], probably the easiest materials of all to handle are zinc sulphide and cryolite. These materials have a good refractive index contrast in the area of interest (around 2.3 for zinc sulphide and 1.3 for the cryolite) and do not compromise the transmission of visible light towards the cell. Besides, they can be easily deposited via thermal evaporation without requiring elevated substrate temperatures. Nonetheless, the low uniformity observed in the films deposited via thermal evaporation is not admissible for the fabrication of multilayer structures.

Compared to this, the most interesting alternative to the current approach lies on the use of silicon nitride and silicon oxide as high and low refractive index materials. As discussed in the previous section, the optical properties of silicon nitride can be easily tuned during the deposition. This is frequently done via PECVD, a widely used method for which a better surface uniformity has been observed.

In addition, it is encouraged that future research focuses on designing a filter able to effectively block infrared light while maximizing the emission of power. During this project, the optical filter design has been mostly aimed at achieving a good reflectance in the area of interest while reducing the number of layers required. However, in order to actually contribute to a significant reduction in the module's operating temperature, the infrared filter must not hamper the emission of light. Otherwise, the unnecessary heating avoided via non absorption could be diminished by a poor radiative exchange with the surroundings. This is particularly true for non-windy locations, in which the infrared filter is expected to make a major contribution. Indeed, in the absence of wind, there is barely no convection around the module and thus radiation becomes the main heat exchange mechanisms.

The previously suggested  $\text{SiN}_x/\text{SiO}_2$  stack is also interesting from this point of view. This is due to the fact that both materials have a strong absorption in the transparency window of atmosphere (between 8 to 13  $\mu\text{m}$ ) [23]. According to *Kirchhoff's law* of thermal radiation, this would imply that the resulting structure would strongly emit in the same area, thus enhancing the radiative heat transfer [74]. However, it should be noted that different techniques have been developed in order to modify the emissivity of materials and hence should also be considered.

## Bibliography

- [1] J. Melorose, R. Perroy, and S. Careas. "World population prospects". In: *United Nations* 1.6042 (2015), pp. 587–92. ISSN: 1098-6596. DOI: [10.1017/CBO9781107415324.004](https://doi.org/10.1017/CBO9781107415324.004). URL: <http://www.ncbi.nlm.nih.gov/pubmed/21798940>.
- [2] U.S. Energy Information Administration (EIA) - Pub. URL: [https://www.eia.gov/forecasts/aeo/section{\\\_}energyconsump.cfm](https://www.eia.gov/forecasts/aeo/section{\_}energyconsump.cfm).
- [3] *Consequences and Effects of Global Warming* | NRDC. URL: <https://www.nrdc.org/stories/are-effects-global-warming-really-bad>.
- [4] International Energy Agency IEA. "Solar Photovoltaic Energy". In: *Technology Roadmap* (2014), p. 60.
- [5] *How Does The Sun Produce Energy? - Universe Today*. 2016. URL: <http://www.universetoday.com/75803/how-does-the-sun-produce-energy/{\#}>.
- [6] Arno Smets et al. *Solar energy: The physics and engineering of photovoltaic conversion, technologies and systems*. 1st. London: UIT Cambridge, 2016.
- [7] ASTM G173 - 03(2012) *Standard Tables for Reference Solar Spectral Irradiances: Direct Normal and Hemispherical on 37° Tilted Surface*. 2012. URL: <https://www.astm.org/Standards/G173.htm>.
- [8] *Standard Solar Spectra* | PVEducation. URL: <http://www.pveducation.org/pvcdrom/appendices/standard-solar-spectra>.
- [9] Fraunhofer Institute for Solar Energy Systems. *Photovoltaics Report: annual Energy Outlook*. 2016.
- [10] Andrea Ingenito. "Opto-electrical surface engineering of wafer based c-Si solar cells". PhD thesis. Delft University of Technology, The Netherlands, 2016. ISBN: 9789463280334.
- [11] Mike Rycroft. *Solar PV module faults and failings - EE Publishers*. 2017. URL: <http://www.ee.co.za/article/solar-pv-module-faults-failings.html>.
- [12] Andrew Blakers et al. "High efficiency silicon solar cells". In: *Energy Procedia* 33 (2013), pp. 1–10. ISSN: 18766102. DOI: [10.1016/j.egypro.2013.05.033](https://doi.org/10.1016/j.egypro.2013.05.033).
- [13] Ran Fu et al. "U.S. Solar Photovoltaic System Cost Benchmark: Q1 2016". In: *National Renewable Energy Laboratory* September (2016), p. 37.
- [14] New Atlas. *Plant openings signal "birth of large-scale solar in Australia"*. 2016. URL: <http://newatlas.com/australia-nyngan-broken-hill-solar-photovoltaic-plants/41462/>.

- [15] PV Resources. URL: <http://www.pvresources.com/>.
- [16] Solar Energy Industries Association. *U.S. Solar Market Has Record-Breaking Year, Total Market Poised to Triple in Next Five Years*. 2017. URL: <http://www.seia.org/news/us-solar-market-has-record-breaking-year-total-market-poised-triple-next-five-years>.
- [17] Union of Concerned Scientists. *Solar Power Plants: Large-Scale PV*. 2015. URL: <http://www.ucsusa.org/clean-energy/renewable-energy/solar-power-plants-large-scale-pv#.WZQP2VFJbIW>.
- [18] U.S. Energy Information Administration (EIA). *More than half of utility-scale solar photovoltaic systems track the sun through the day*. 2017. URL: <https://www.eia.gov/todayinenergy/detail.php?id=30912>.
- [19] R. Santbergen. "Optical Absorption Factor of Solar Cells for PVT Systems". PhD thesis. Eindhoven University of Technology, The Netherlands, 2008.
- [20] Alok Sahu, Neha Yadav, and K Sudhakar. "Floating photovoltaic power plant: A review". In: *Renewable and Sustainable Energy Reviews* 66 (2016), pp. 815–824.
- [21] Mark Osborne. *China completes largest floating solar power plant*. 2017. URL: <https://www.pv-tech.org/news/china-completes-largest-floating-solar-power-plant>.
- [22] Solimpeks Solar Energy Corp. *Volther Powertherm*. URL: <http://www.solimpeks.com/product/volther-powertherm/>.
- [23] Aaswath P Raman et al. "Passive radiative cooling below ambient air temperature under direct sunlight." In: *Nature* 515.7528 (2014), pp. 540–4.
- [24] Wei Li et al. "A Comprehensive Photonic Approach for Solar Cell Cooling". In: *ACS Photonics* 4.4 (2017), pp. 774–782.
- [25] T. L. Bergman and Frank P. Incropera. *Fundamentals of heat and mass transfer*. Wiley, 2011.
- [26] Robert G. Mortimer. *Physical chemistry*. Academic Press/Elsevier, 2008, p. 1395.
- [27] Latif M. (Latif Menashi) Jiji. *Heat convection*. Springer, 2009, p. 543.
- [28] W.H. McAdams. *Heat Transmission*. Third ed. New York: McGraw-Hill, 1954.
- [29] J. H. Watmuff, W. W. S. Charters, and D Proctor. *Solar and wind induced external coefficients - Solar collectors*. Tech. rep. 1977, p. 56.
- [30] P.J. Lunde. *Solar thermal engineering: Space heating and hot water systems*. Wiley and Sons, 1980.
- [31] E M Sparrow, J W Ramsey, and E A Mass. "Effect of Finite Width on Heat Transfer and Fluid Flow about an Inclined Rectangular Plate". In: *Journal of Heat Transfer* 101.2 (May 1979), pp. 199–204.
- [32] F L Test, R C Lessmann, and A Johary. "Heat transfer during wind flow over rectangular bodies in the natural environment". In: *Journal of Heat Transfer* 103.2 (1981), pp. 262–267.
- [33] R.J. Cole and N.S. Sturrock. "The convective heat exchange at the external surface of buildings". In: *Building and Environment* 12.4 (1977), pp. 207–214.
- [34] S. Sharples and P.S. Charlesworth. "Full-scale measurements of wind-induced convective heat transfer from a roof-mounted flat plate solar collector". In: *Solar Energy* 62.2 (1998), pp. 69–77.

- [35] S Armstrong and W G Hurley. "A thermal model for photovoltaic panels under varying atmospheric conditions". In: *Applied Thermal Engineering* 30.11-12 (2010), pp. 1488–1495.
- [36] Rudi Santbergen. *Manual for solar cell optical simulation software: GenPro4*. Tech. rep. February. Delft University of Technology, 2016.
- [37] Nyanor Peter et al. "3D Finite Element Method Modeling and Simulation of the Temperature of Crystalline Photovoltaic Module". In: (2015), pp. 378–384.
- [38] Silvano Vergura, Giuseppe Acciani, and Ottavio Falcone. "A finite-element approach to analyze the thermal effect of defects on silicon-based PV cells". In: *IEEE Transactions on Industrial Electronics* 59.10 (2012), pp. 3860–3867. ISSN: 02780046.
- [39] Martin K Fuentes. "A Simplified Thermal Model for Flat-Plate Photovoltaic Arrays". In: *Sandia Report* (1987), p. 60.
- [40] Christian Vogt, Norbert Klitzsch, and Volker Rath. "On self-potential data for estimating permeability in enhanced geothermal systems". In: *Geothermics* 51 (July 2014), pp. 201–213. ISSN: 03756505. DOI: [10.1016/j.geothermics.2014.01.008](https://doi.org/10.1016/j.geothermics.2014.01.008). URL: <http://www.sciencedirect.com/science/article/pii/S0375650514000091>.
- [41] Malte Ruben Vogt. "Development of Physical Models for the Simulation of Optical Properties of Solar Cell Modules". PhD thesis. Leibniz Universität Hannover, Germany, 2015, pp. 124–131.
- [42] Meteororm. *Meteororm: Irradiation data for every place on Earth*. URL: <http://www.meteororm.com/>.
- [43] Arianna Tozzi. *The Dutch Photovoltaic Energy Portal (MSc thesis)*. Tech. rep. Delft University of Technology, The Netherlands, 2014.
- [44] Britannica. *Snell's law - physics*. 2017. URL: <https://www.britannica.com/science/Snells-law>.
- [45] Juan Camilo Ortiz Lizcano. *Optic Filters for Built-integrated Photovoltaic (BIPV) applications (MSc thesis)*. Tech. rep. Delft University of Technology, The Netherlands, 2014, p. 110.
- [46] H. A. Macleod. *Thin-Film Optical Filters*. Third ed. Tucson, Arizona: Institute of Physics Publishing, 2001.
- [47] Boundless. *Interference and Diffraction*. May 2016. URL: <https://www.boundless.com/chemistry/textbooks/boundless-chemistry-textbook/introduction-to-quantum-theory-7/the-nature-of-light-63/interference-and-diffraction-295-3665/>.
- [48] *Optical Filters Information | Engineering360*. URL: [http://www.globalspec.com/learnmore/optical{\\\_}components{\\\_}optics/optical{\\\_}components/optical{\\\_}filters](http://www.globalspec.com/learnmore/optical{\_}components{\_}optics/optical{\_}components/optical{\_}filters).
- [49] *What is a Dichroic Filter? : Abrisa Technologies*. URL: <http://abrisatechnologies.com/2014/10/what-is-a-dichroic-filter/>.
- [50] *Dichroic filters*. URL: <http://www.knightoptical.com/stock/optical-components/uvvisnir-optics/filters/dichroic-filters/>.
- [51] *Wavelength Selection Filters : Abrisa Technologies*. URL: <http://abrisatechnologies.com/products-services/coating-solutions/coatings-capabilities/wavelength-selection-filters/>.

- [52] Olindo Isabella. "Light Management in thin-film silicon solar cells". PhD thesis. Delft University of Technology, The Netherlands, 2013.
- [53] Hayder Touran Assafli, Ali Hameed, and Wail Nassir. "Design High Efficient Reflectivity of Distributed Bragg Reflectors". In: *Iraqi Journal of Laser* 15 (2016), pp. 15–20.
- [54] J Krc et al. "Modulated photonic-crystal structures as broadband back reflectors in thin-film solar cells". In: *Applied Physics Letters* 94.15 (2009), p. 153501.
- [55] Alexander Tikhonravov and Michael Trubetskov. "Thin film coatings design using second order optimization methods". In: *Thin Film for Optical Systems* 1782.1 (1992), pp. 156–164.
- [56] Alexander V. Tikhonravov, Michael K. Trubetskov, and Gary W. Debell. "Application of the needle optimization technique to the design of optical coatings." In: *Applied optics* 35.28 (1996), pp. 5493–508.
- [57] Stéphane Larouche and Ludvik Martinu. "OpenFilters: open-source software for the design, optimization, and synthesis of optical filters". In: *Applied Optics* 47.13 (May 2008), p. C219.
- [58] Alaa Nazar. "Design optical filters using two different synthesis approaches". In: *Journal of Kufa* 3.1 (2011).
- [59] Ronald R Willey. "Using fence post designs to speed the atomic layer deposition of optical thin films." In: *Applied optics* 47.13 (2008), pp. C9–C12.
- [60] R. R. Willey. "Design of Optical Thin Films Using the Fencepost Method". In: (2007), pp. 365–368.
- [61] G. Yang. "High-efficient n-i-p thin-film silicon solar cells". PhD thesis. Delft University of Technology, The Netherlands, 2015.
- [62] PennState Materials Research Institute. *Ultraviolet Visible Spectroscopy (UV-Vis-NIR) Instrumentation*. URL: <https://www.mri.psu.edu/materials-characterization-lab/characterization-techniques/ultraviolet-visible-spectroscopy-uv-vis>.
- [63] Ming-Chung Liu et al. "Microstructure of magnesium fluoride films deposited by boat evaporation at 193 nm." In: *Applied optics* 45.28 (2006), pp. 7319–7324.
- [64] Seouk-Hoon Woo and Chang Kwon Hwangbo. "Effects of annealing on the optical, structural, and chemical properties of TiO<sub>2</sub> and MgF<sub>2</sub> thin films prepared by plasma ion-assisted deposition". In: *Appl. Opt.* 45.7 (2006), pp. 1447–1455.
- [65] Nicolas Martin et al. "Microstructure modification of amorphous titanium oxide thin films during annealing treatment". In: *Thin Solid Films* 300.1-2 (1997), pp. 113–121.
- [66] B. S. Richards. "Single-material TiO<sub>2</sub> double-layer antireflection coatings". In: *Solar Energy Materials and Solar Cells* 79.3 (Sept. 2003), pp. 369–390.
- [67] Marius Peters et al. "Spectrally-Selective photonic structures for PV applications". In: *Energies* 3.2 (2010), pp. 171–193.
- [68] W. W. Rigrod, G Skelly, and Oscillator Mirrors. "Suppression of Reflection Peaks in Passbands of Multilayer Dielectric Filters". In: *Applied Optics* 10.2 (1971), pp. 311–316.
- [69] Xia Yan, Selvaraj Venkataraj, and Armin G. Aberle. "Modified surface texturing of aluminium-doped zinc oxide (AZO) transparent conductive oxides for thin-film silicon solar cells". In: *Energy Procedia* 33 (2013), pp. 157–165.

- [70] Seouk-Hoon Woo, Sung-Hwa Kim, and Chang Kwon Hwangbo. "Plasma ion-assisted deposition of TiO<sub>2</sub> and MgF<sub>2</sub> thin films". In: *Journal of the Korean Physical Society* 45.1 (2004), pp. 99–107.
- [71] George Atanassov et al. "Mechanical , optical and structural properties of TiO<sub>2</sub> and MgF<sub>2</sub> thin films deposited by plasma ion assisted deposition". In: 342 (1999), pp. 83–92.
- [72] John W. Hutchinson. *Stresses and failure modes in thin films and multilayers*. Tech. rep. Cambridge, MA, USA: Division of Engineering and Applied Sciences, Harvard University, 1996, pp. 1–45.
- [73] Sadanand V. Deshpande et al. "Optical properties of silicon nitride films deposited by hot filament chemical vapor deposition". In: *Journal of Applied Physics* 77.12 (1995), pp. 6534–6541.
- [74] Yanguo. Zhang, Qinghai. Li, and Hui. Zhou. *Theory and calculation of heat transfer in furnaces*. London: Academic Press, 2016.